1   **Revision 2**

2   Word Count: 9088

3   **Scheelite composition fingerprints pulsed flow of magmatic fluid in**

4   **the Fujiashan W skarn deposit, eastern China**

5

6

7   YunHao Ji[1,2], GuiQing Xie[1,2*], Rolf L. Romer[3], Wei Li[1,2], QiaoQiao Zhu[4], Bin Fu[5]

8

9

10   *1 School of Earth Sciences and Resources, China University of Geosciences, Beijing*

11   *100083, China*

12   *2 MNR Key Laboratory for Exploration Theory & Technology of Critical Mineral*

13   *Resources, China University of Geosciences, Beijing, 100083, China*

14   *3 Inorganic and Isotope Geochemistry, GFZ German Research Centre for*

15   *Geosciences, Telegrafenberg, D-14473 Potsdam, Germany*

16   *4 MNR Key Laboratory of Metallogeny and Mineral Assessment, Institute of Mineral*

17   *Resources, CAGS, Beijing 100037, China*

18   *5 Research School of Earth Sciences, The Australian National University, Canberra,*

19   *ACT 2601, Australia*

20

21

22

23

24   Corresponding author E-mail address: xieguiqing@cugb.edu.cn

25   **ABSTRACT**

26   Scheelite ($CaWO_4$) is an economically important W mineral in skarns that form when

27   magmatic fluids exsolved from a granitic intrusion react with carbonate wall rocks. In

28   the Fujiashan W skarn deposit scheelite formed during all four stages of the

29   hydrothermal skarn development. We present cathodoluminescence (CL) images and

30   in-situ trace element and Sr-O isotope data of scheelite from these four stages, i.e.,

31   scheelite in prograde and retrograde skarn, quartz-sulfide veins, and late calcite

32   replacements. Scheelite from prograde skarn and quartz sulfide veins are

33   homogeneous and show oscillatory zoning textures in CL images, whereas scheelite

34   from retrograde skarn and late carbonate stages display dissolution-reprecipitation and

35   patchy textures. The brightness of CL textures decrease with higher substitution of

36   Mo. Molybdenum-rich scheelite (up to 2.1 wt%) is characterized by relatively high

37   contents of Nb and Ta (up to 156 and 0.9 ppm, respectively), positive Eu anomalies,

38   high $\delta^{18}O$ values (5.2 to 5.9 ‰), and relatively low $^{87}Sr/^{86}Sr$ values (0.70661 to

39   0.70727), and has grown in a system with a continuous supply of magmatic fluid.

40   Molybdenum-poor scheelite (0.2 wt%) has low contents of Nb and Ta, negative Eu

41   anomalies, low $\delta^{18}O$ values (4.2 to 4.3 ‰) and relatively high $^{87}Sr/^{86}Sr$ ratios (0.70748

42   to 0.70804). This type of scheelite formed in a system with restricted flow of

43   magmatic fluid that during scheelite precipitation became increasingly depleted in

44   elements that substitute into scheelite. The continued reaction of the magmatic fluid

45   with the wall rocks and the precipitation of minerals from the fluid resulted in a

46   systematic change of the $\delta^{18}O$ and $^{87}Sr/^{86}Sr$ ratios. Chemical and isotopic variations in

47   scheelite may reflect pulsed flow of a magmatic fluid and do not require the

48   involvement of different fluids or contrasting redox conditions.

49

50   **Keywords:** Scheelite, Trace element, In-situ Sr-O isotope analysis, Pulsed magmatic

51   fluid, Skarn

52

53   **INTRODUCTION**

54   Skarn deposits are important sources of Sn, W, Cu, Pb, Zn, and high-grade Fe ores

55   (e.g., Chang et al. 2019). Skarns are dominated by calc-silicate minerals such as

56   garnet, pyroxene, and wollastonite and formed by interaction of magmatic-

57   hydrothermal fluids emanating from granitic intrusions with carbonate wall rocks (e.g.,

58   Meinert et al. 2005). Commonly, magmatic-hydrothermal fluids migrate along

59   silicate-rich layers and fractures that act as aquifers within the carbonate rocks,

60   whereas the carbonate rock act as aquitards. Consumption of aquifer and aquitard

61   during the formation of skarn minerals increases the permeability, which focuses fluid

62   flow and promotes additional reaction. The reaction-induced increase of permeability

63   is counteracted by the ambient pressure that reduces the interconnectivity of the pores

64   and eventually results in episodic fluid flow (e.g., Cui et al. 2001; Milsch et al. 2003).

65   Reaction-induced changes of the fluid composition induce precipitation of

66   economically relevant elements by formation of ore minerals, e.g., W in scheelite, or

67   substitution in gangue minerals, e.g., Sn in skarn silicates (e.g., Lefebvre et al., 2019).

68   Traditionally, the source and evolution of mineralizing fluids in skarn deposits

69   have been studied using O isotope data of bulk gangue mineral separates and

70   hydrogen isotope data of fluid inclusions in gangue minerals (Taylor et al. 1977; Lu et

71   al. 2003). In-situ O isotope data of gangue minerals show that the fluid composition

72   may vary during the evolution of the hydrothermal system and mineralization

73   (D'Errico et al. 2012; Ryan-Davis et al. 2019; Li et al. 2022a; Liu et al., 2023). It can

74   be difficult, however, to link variations in the compositions of gangue minerals with

75   the precipitation of ore minerals. Using the compositional variation of ore minerals as

76   a monitor of changing fluid composition and fluid source, as well as changing

77   precipitation conditions, is an approach that removes the uncertainty of the genetic

78   relation between gangue and ore minerals. In W skarn deposits, scheelite seems to be

79   particularly well suited to trace fluid evolution and fluid sources as crosscutting

80   relations and alteration assemblages indicate that scheelite may form during both

81   prograde and retrograde stages (Poulin et al. 2018; Miranda et al. 2022). Due to

82   similar electron configurations and ionic radii, rare earth elements (REE), Sr, and Y

83   readily enter the scheelite structure, substituting for Ca^{2+} (Raimbault et al., 1993;

84   Poulin et al. 2018), whereas higher charged elements may substitute for W^{6+}. The

85   chemical inventory of scheelite is derived from different sources, i.e., Ca and Sr from

86   the carbonate wall rocks, Si, Al, and other major elements from the aquifer or silicate

87   minerals within the carbonate rocks, and W, alkali elements, and REE from the

88   magmatic-hydrothermal fluids. The availability of these elements may vary in the

89   course of the development of the skarn (Poulin et al. 2018; Sun et al. 2019). Therefore,

4

90   variations in the trace element contents of scheelite reflect progressive fluid-rock

91   interaction during the formation of a W skarn deposit. $\delta^{18}O$ and $^{87}Sr/^{86}Sr$ may trace

92   the source of the fluid and record the interaction of the ore-forming fluid with the wall

93   rocks (Sun et al. 2017; Song et al. 2019; Li et al. 2021a). The ubiquitous overprint and

94   multi-stage growth of scheelite implies that bulk analysis provides mixed signatures

95   from multiple processes, whereas in-situ Sr-O isotope data may distinguish different

96   stages of a dynamic ore-forming process.

97   In this paper, we focus on scheelite in the Fujiashan W skarn deposit, an oxidized

98   W deposit at the Edong ore cluster, eastern China (Ji et al. 2019). We demonstrate

99   grain-scale variation of in-situ trace element and Sr-O isotope data in scheelite,

100   highlighting the behavior of scheelite-compatible trace elements during fluid-rock

101   interaction. Furthermore, we characterize the source and evolution of ore-forming

102   fluids at different stages.

103   GEOLOGICAL SETTING

104   The Middle-Lower Yangtze River Metallogenic Belt (MLYRB) is located at the

105   northern margin of the Yangtze Craton and borders the southeastern margin of the

106   North China Craton and the Dabieshan orogenic belt (Fig. 1; Zhai et al. 1996; Mao et

107   al. 2011). The MLYRB contains seven ore districts, including from west to east, the

108   Edong, Jiurui, Anqing-Guichi, Luzong, Tongling, Ningwu, and Ningzhen districts

109   (Chang et al. 1991; Pan and Dong 1999; Mao et al. 2011) (Fig. 1b). The MLYRB is

110   bounded by the Xiangfan–Guangji Fault (XGF) to the northwest, the regional strike–

5

111 slip Tancheng–Lujiang Fault (TLF) to the northeast, and the Yangxin–Changzhou

112 Fault (YCF) to the south (Fig. 1b). The MLYRB is characterized by an Archean–

113 Proterozoic metamorphic basement overlain by Cambrian to Early Triassic marine

114 sedimentary rocks and Middle Triassic to Cretaceous terrigenous clastic and volcanic

115 rocks (Zhai et al. 1996; Mao et al. 2011). Major mineralization and magmatism of the

116 MLYRB includes three groups (Mao et al. 2011; Zhou et al. 2015). The first group

117 includes 156–136 Ma diorites, granodiorites, and granodiorite porphyries with

118 porphyry-skarn Cu-Au-Mo deposits; The second group includes 135–123 Ma

119 gabbros, diorites, quartz diorites, quartz monzonites, granites, and diorite porphyries

120 with magnetite-apatite deposits and Fe skarn deposits. The third group comprises

121 127–123 Ma A-type quartz syenites, syenites, and alkaline granites with minor gold

122 and uranium mineralization.

123 In the Edong Fe-Cu ore district, Cambrian to middle Triassic marine carbonate and

124 clastic rocks and flysch successions are widespread. There are two groups of

125 Mesozoic granitoids with related mineralization that were emplaced into these

126 sedimentary rocks (Xie et al. 2011; Li et al. 2014). The older group includes

127 granodiorites and granites with 147–136 Ma Cu-Au-Mo, and W porphyry-skarn

128 deposits and 144–143 Ma Cu-Fe and Fe-Cu skarn deposits. The younger group

129 includes 133–127 Ma diorites, granites, and monzonitic granites with Fe skarn

130 deposits. Three W deposits from the Edong district have been mined, ie., the

131 Tongshankou, Ruanjiawan and Fujiashan deposits (Fig. 1c).

6

132   GEOLOGY OF THE FUJIASHAN DEPOSIT

133   The Fujiashan W skarn deposit is located in the southern part of the Edong ore district

134   (Fig. 1c). It is the largest oxidized W skarn deposit in this district and has proven

135   reserves of 58,000 tons WO$_3$, 14,000 tons Cu, 5,800 tons Mo at average ore grades of

136   0.27% WO$_3$, 0.77% Cu, and 0.1% Mo (Ji et al. 2019). The Fujiashan deposit includes

137   two ore segments at the eastern and western contact zones of the early Cretaceous

138   granodiorite porphyry, respectively (Fig. 2). The western ore segment, which accounts

139   for 75 % of the W resource reserves in the Fujiashan deposit, hosts 19 NW-striking

140   lenticular, planar, and layered orebodies. The eastern ore segment hosts 8 NE-striking

141   lenticular, tabular, and platy orebodies. The largest orebody is 520 m long, on average

142   35 m wide, and documented to depths of 578 m. The zircon U-Pb age of granodiorite

143   porphyry and the molybdenite Re-Os age of skarn are 144 ± 3 Ma and 146 ± 2 Ma,

144   respectively (Liu et al. 2021). The granodiorite porphyry is composed of plagioclase

145   (~40%), quartz (~10%), K-feldspar (~5%), and biotite (~5%) phenocrysts and

146   groundmass of plagioclase, quartz, biotite, and hornblende (Figs. 3a, b). The wall

147   rocks of the ore segments are limestones of the Permian Maokou and Qixia

148   formations (Fig. 2a).

149   Hydrothermal alteration is extensive in the Fujiashan deposit, including skarn,

150   sulfide, and carbonate alterations. Endoskarn is absent in the Fujiashan deposit and

151   the extensively developed exoskarn is garnet skarn with a distinct color zoning

152   ranging from dark brown (Fig. 3c) in the proximal section to light brown (Fig. 3e),

153   red-dark green (Fig. 3g), and orange sections (Fig. 3i) towards the marble front. The

7

154   proximal exoskarn is dominated by garnet and pyroxene, whereas vesuvianite and

155   wollastonite occur mainly at the contact between skarn and marble. Based on field

156   appearance, mineral assemblage, alteration, and ore textures/structures, four stages of

157   mineralization can be distinguished, i.e., (1) prograde skarn, (2) retrograde skarn, (3)

158   quartz-sulfide alteration, and (4) carbonate alteration.

159   *Stage 1: prograde skarn*

160   The prograde skarn stage is characterized by abundant garnet and pyroxene, and

161   minor wollastonite. Garnet, 0.02 to 3 mm in diameter, forms euhedral to subhedral

162   crystals that in part are overgrown by euhedral pyroxene (Fig. 3f). The composition of

163   garnet varies along the grossularite-andradite solid solution and ranges from

164    $And_{66\sim95}Gro_{0\sim27}Spr_{3\sim7}$ to $And_{19\sim33}Gro_{60\sim76}Spr_{3\sim7}$ (Ji et al. 2019). The composition of

165   euhedral to subhedral, 0.01 to 2 mm long pyroxene crystals fall on the diopside-

166   hedenbergite solid solution, ranging from $Di_{44\sim64}Hd_{29\sim49}$ to $Di_{0\sim100}Hd_{0\sim97}$ (Ji et al.

167   2019). The compositions of garnet and pyroxene from the Fujiashan deposits broadly

168   overlap the corresponding ranges from other oxidized W skarn deposits (Einaudi et al.

169   1981; Meinert et al. 2005). Rounded to euhedral scheelite crystals, 0.1 to 0.3 mm in

170   diameter, occur as isolated inclusions within garnet or are intergrown with pyroxene

171   (Figs. 3d, h). Scheelite in prograde skarn shows yellow fluorescence under ultraviolet

172   light.

173   *Stage 2: retrograde skarn*

174   Retrograde skarn is dominated by epidote, chlorite, and minor actinolite, apatite,

175   and titanite. Epidote and chlorite are subhedral, ranging from 0.1 to 1 mm and 0.1 to

8

176   0.2 mm in size, respectively, and are locally replaced by pyrite and calcite (Fig. 4k).

177   Retrograde alteration of the garnet skarn resulted in more intense W mineralization.

178   Euhedral to subhedral scheelite grains that formed in this stage are coarse-grained (0.2

179   to 2 mm) and occur together with the hydrous minerals chlorite and actinolite (Fig. 4l).

180   Scheelite from this stage has yellow fluorescence under ultraviolet light.

181   *Stage 3: quartz-sulfide alteration*

182   This stage is characterized by abundant scheelite, pyrite, chalcopyrite, quartz,

183   magnetite, and minor sphalerite and galena (Fig. 4m). The quartz-scheelite veins and

184   quartz-sulfide veins with epidote halos crosscut garnet skarn (Figs. 4a, f). Pyrite and

185   chalcopyrite form euhedral to subhedral crystals that have 0.1 to 4 mm diameter.

186   Quartz fills fractures in garnet and forms veins cutting the garnet skarn (Fig. 4g).

187   Most Cu and Mo mineralization developed at this stage (Figs. 4h, i). Subhedral

188   chalcopyrite crystals, 0.1 to 1 mm in diameter, commonly occur together with

189   scheelite and pyrite (Fig. 4n). Molybdenite, replacing garnet skarn, forms crystals

190   with 0.1 to 1 mm diameter (Fig. 4i). Scheelite crystals of this stage have 0.1 to 3 mm

191   diameter and may show yellow to blue fluorescence within individual crystals under

192   ultraviolet light (Figs. 4b, c).

193   *Stage 4: carbonate alteration*

194   This stage is characterized by calcite with minor quartz, sulfide, and scheelite.

195   Typically, calcite forms massive aggregates that replace garnet and epidote (Fig. 4e).

196   Scheelite crystals of this stage have 0.2 to 3 mm diameter and have blue fluorescence

197   under ultraviolet light (Fig. 4d).

9

<div align="center">

SAMPLES AND ANALYTICAL METHOD

</div>

198

199   Representative scheelite-bearing hand-specimens were collected from five drill cores

200   that were taken along a northwest-southeast trending section covering all stages of W

201   mineralization (Fig. 2a; Appendix Table S1). Each sample was prepared as polished

202   thin section (30–40 μm thick) and investigated using reflected and transmitted light

203   microscopy to characterize the mineralogy, paragenetic relationships, and

204   hydrothermal alteration.

205   **Cathodoluminescence (CL) imaging**

206   Scheelite CL images were obtained using a Gatan MonoCL 4 system attached to the

207   FEI Nova NanoSEM 450 scanning electron microscope (FEI corporation, Hillsboro,

208   OR, USA) at the Institute of Geology, Chinese Academy of Geological Sciences,

209   Beijing.

210   **Trace elements spot and mapping analysis**

211   Trace element spot analysis and mapping of scheelite were done using a laser ablation

212   system (PhotonMachines Analyte HE with 193-nm ArF Excimer), coupled to a

213   quadrupole-based inductively coupled plasma mass spectrometer (ICP-MS, Agilent

214   7900), at the Ore Deposit and Exploration Centre, School of Resources and

215   Environmental Engineering, Hefei University of Technology. Monitored isotopes

216   included ^{23}Na, ^{82}Pb, ^{88}Sr, ^{89}Y, ^{93}Nb, ^{95}Mo, ^{139}La, ^{140}Ce, ^{141}Pr, ^{146}Nd, ^{147}Sm, ^{153}Eu,

217   ^{157}Gd, ^{159}Tb, ^{163}Dy, ^{165}Ho, ^{166}Er, ^{169}Tm, ^{172}Yb, ^{175}Lu, ^{181}Ta, ^{185}Re, and ^{238}U. Trace

218   element analysis uses 20~35 μm spot size, ~2 J/cm^2 laser fluence, and 8 Hz repetition

219   rate. Each spot analysis includes of 20s background acquisition before and after 30s

10

220   data acquisition. Standard reference materials BCR-2G, SRM 610 and SRM 612 were

221   used as external standards. The composition of these reference materials used as

222   secondary standards are given in Appendix Table S2. Element contents were

223   calibrated using multiple external standards and without internal standard (Liu et al.

224   2008). The average detection limits are given in Appendix Table S2.

225   For trace element mapping, we used 15~40 μm spot size, 2 J/cm^2 energy density

226   and 15~40 μm/s scan speed. Standard materials NIST-610 (Jochum et al. 2011) and

227   GSD-1G (Guillong et al. 2005) were analyzed for data calibration at the start and end

228   of each mapping run. LA-ICP-MS trace element images were compiled and processed

229   using the program LaIcpMsSoftWare2.2, an in-house designed mapping reduction

230   software based on Matlab.

231   **In-situ Sr isotope analysis**

232   In-situ Sr isotope measurements were performed using a Neptune Plus MC-ICP-MS

233   (Thermo Fisher Scientific, Germany) in combination with a femtosecond laser at the

234   National Research Center for Geoanalysis, Chinese Academy of Geological Sciences

235   (CAGS), Beijing, China. Helium gas carried the ablated sample aerosol from the

236   ablation chamber was mixed with argon make-up gas and nitrogen to enhance

237   sensitivity. The instrumental mass bias for the Sr isotopic composition was corrected

238   using an exponential law and normalizing to the ^{86}Sr/^{88}Sr ratios of 0.1194. Samples

239   were ablated in line mode with a spot size of 40 μm and a line length of 20 μm. The

240   in-house scheelite references (XJSW) were analyzed after each set of 10 analyzes of

241   unknowns to correct for drift (Li et al. 2018). The ^{87}Sr/^{86}Sr ratios of XJSW is

242   0.720867 ± 0.000021 (2SE). The data obtained for this reference material using our

243   analytical setup are given in Appendix Table S3. Scheelite Sr isotope data and

244   uncertainties of $^{87}Sr/^{86}Sr$ ratios (2SE) are given in full as Appendix Table S3.

245   **In-situ O isotope analysis**

246   Chips of polished thin sections and in-house reference materials (YJS66 Scheelite;

247   4.5 ‰; Li et al. 2021b) were cast into an epoxy disk, ground, and polished. Oxygen

248   isotope ratios ($^{18}O/^{16}O$) of scheelite were determined using a SHRIMP SI ion

249   microprobe at the Research School of Earth Sciences, the Australian National

250   University (Canberra). Analytical conditions were similar to those of Ávila et al.

251   (2020). The elliptical beam spot had an average diameter of 25 μm. Typically, 3–5

252   analyses of unknowns were bracketed by 1 or 2 analyses of the standard material.

253   Calibrated $^{18}O/^{16}O$ ratios are reported in $\delta^{18}O$ notation relative to Vienna standard

254   mean ocean water (VSMOW). The data for primary standard YJS66 Scheelite are

255   shown in Appendix Table S4. The average external (spot-to-spot) reproducibility, as

256   estimated from replicate measurements of the scheelite standard, is better than ± 0.60 ‰

257   (2SD). The O isotope composition of the fluid in equilibrium with scheelite was

258   calculated using the fractionation factors: 1000lnα scheelite-water $=1.39 \times 10^6/T^2 -$

259   5.87 (Wesolowski and Ohmoto 1986) and the temperatures obtained from fluid

260   inclusions. Fluid temperatures vary from 500 °C in prograde skarn to 375 °C in

261   retrograde skarn, 275 °C in quartz-sulfide alteration, and 200°C in carbonate

262   alteration (Lei et al. 2018). The results are summarized in Table 3 and Appendix

263   Table S4.

12

264 **RESULTS**

265 **Scheelite textures**

266 Based on replacement relationships, textural features and CL images, scheelite of the

267 four stages of mineralization can be distinguished into homogeneous, patchy and

268 oscillatory zoned sub-types.

269 Scheelite from Stage 1 is intergrown with garnet in the proximal zone near the

270 contact between skarn and granodiorite porphyry and can be distinguished into two

271 sub-types. Sch1a is shows homogeneous texture (Figs. 3d and 5a), whereas Sch1b

272 displays an oscillatory zoning texture (Figs. 3h and 5b).

273 Scheelite from Stage 2 shows oscillatory zoning in the core (Sch 2a, Fig. 5c) and

274 has homogenous CL in the rim (Sch 2b, Fig. 5d). The contact between Sch2a and

275 Sch2b may show truncations of the zoning pattern, which is indicative of dissolution-

276 reprecipitation (Fig. 5d). Sch2a and Sch2b commonly coexist with hydrous minerals,

277 such as chlorite, epidote, and actinolite.

278 Scheelite from Stage 3 displays two different sub-types in CL images. Sch3a exists

279 in quartz-sulfide veins and commonly displays oscillatory zonation defined by

280 multiple zones that may reach several tens of micrometers width (Figs. 5e, f), whereas

281 Sch3b exists in high-grade W ore and shows a homogeneous texture (Fig. 5g).

282 Scheelite from Stage 4 mainly coexist with calcite, which is characterized by a

283 well-developed oscillatory zoning pattern in the core (Sch4a, Figs. 5h, i) and a patchy

284 texture at the rim (Sch4b, Fig. 5h). The contact boundary between Sch4a and Sch4b is

285 irregular (Fig. 5h).

286 **Trace element compositions**

287 Representative trace element compositions for the various scheelite are summarized in

288 Tables 1 and 2 and shown in Figs. 6 and 7. The full data set is given in Appendix

289 Table S2.

290 The contents of Sr in scheelite fall in the range from 85 to 440 ppm (Tables 1 and

291 2). The ranges of Sr contents of the various sub-types broadly overlap and show

292 within each group a general tendency to higher Sr contents with time (Fig. 6a). Only

293 Sch2a and Sch4b deviate from this pattern. Sch2a from the retrograde skarn seems to

294 have slightly higher Sr contents than scheelite from the prograde skarn and quartz-

295 sulfide alteration. Sch4b from calcite alteration represents the youngest type and has

296 the highest Sr contents.

297 The concentrations of Mo, Nb+Ta, and total REE in scheelite show systematic

298 variations. For each mineralization stage, early scheelite has higher and more variable

299 contents of these metals than late scheelite (Fig. 6, Table 1). Furthermore, the contents

300 of Mo and Nb+Ta of scheelite in prograde and retrograde skarn seem to be more

301 variable and higher than in scheelite from quartz-sulfide veins and calcite alterations.

302 Scheelite from the Fujiashan W skarn deposit has high Mo contents, which accounts

303 for yellow fluorescence under ultraviolet light. The highest Mo contents are observed

304 in scheelite from the prograde and retrograde skarn and may reach 5 and 7 wt%,

305 respectively. For comparison, the contents of Nb+Ta reach up to 180 ppm (Figs. 6b,

306 c). The highest total REE contents are observed in scheelite from prograde skarn and

307 quartz-sulfide veins with up to 945 and 1103 ppm, respectively, whereas the lowest

14

308   total REE contents are found for in scheelite from the calcite stage with only 97 ppm

309   (Fig. 6d).

Trace element mapping

311   Trace-element mapping is used to visualize the distribution of chemical elements in

312   Sch3a with oscillatory zoning. High Mo contents result in lower intensity of the CL

313   response of scheelite. The element mapping reveals that trace elements are irregularly

314   distributed in different zones. Most trace elements in scheelite are enriched in the

315   inner zone, depleted in the transition zone, and enriched in the scheelite rim. The

316   contents of total REE, Nb+Ta, Sr, Y, Nd, and La in general show the same pattern as

317   the CL response of scheelite (Fig. 8). The distribution of Eu and Sr does not show the

318   same chemical zoning as the other elements (e.g., Nd, Nb+Ta, Y, total REE).

Sr and O isotope composition

320   The Sr isotope data for scheelites from the Fujiashan deposit are summarized in Table

321   3 and Appendix Table S3. The data were taken along profiles from core to rim in

322   individual scheelite grains and represent the temporal variation from early to late

323   stages. For each mineralization stage, early scheelite has lower Sr isotope ratios than

324   late scheelite, except for scheelite from Stage 3 (Fig. 9). The ^{87}Sr/^{86}Sr ratios of Sch1a

325   and Sch1b range from 0.70682 to 0.70770 and 0.70706 to 0.70811, respectively. In

326   Sch2, the ^{87}Sr/^{86}Sr ratios of the core (0.70663–0.70735) are lower than those of the

327   rim (0.70749–0.70772). The ^{87}Sr/^{86}Sr ratios of Sch3a are higher than Sch3b, ranging

328   from 0.70661 to 0.70804 and 0.70697 to 0.70720, respectively, i.e., encompass the

329   entire range from the granodioritic source of the magmatic fluids to the wall rocks, i.e.,

330   the carbonates of the Qixia Formation (0.70734–0.70821). The last generation of

331   scheelite Sch4b, however, seems to reach even higher $^{87}Sr/^{86}Sr$ ratios (0.70853–

332   0.70855) (Fig. 9), possibly reflecting that locally high contents of silicate minerals in

333   the carbonate sediments account for these high $^{87}Sr/^{86}Sr$ ratios.

334   The $\delta^{18}O$ values show a general decrease from early to late crystallized scheelite

335   for stages 1, 2 and 4, whereas scheelite from Stage 3 shows the opposite trend.

336   Scheelite Sch1a, Sch1b, Sch2a and Sch3b have values that fall in the range of the

337   magmatic fluid, with $\delta^{18}O_{fluid}$ values ranging from 8.27 to 9.56 ‰ for Sch1a and from

338   7.15 to 9.09 ‰ for Sch2a. The other scheelite samples have $\delta^{18}O$ values below the

339   range of the magmatic fluid, the lowest $\delta^{18}O_{fluid}$ value for Sch 4b (–10.86 to –9.05 ‰)

340   falling in the range of meteoric water (Fig. 10).

341   **Trace element contents and isotope compositions within individual scheelite**

342   **crystals**

343   The oscillatory zoning in scheelite reflects a multi-generation growth history with

344   core to rim variations in trace element contents and the Sr and O isotopic

345   compositions. For example, The Nb contents of stage 3 scheelite decrease from 8.6 to

346   2.5 ppm (Fig. 11b). The δEu and Mo contents of scheelite gradually decrease from 1.9

347   to 0.8 and 8300 to 494 ppm from core to rim, respectively, whereas the $^{87}Sr/^{86}Sr$ ratios

348   increase from 0.70674 to 0.70794 (Figs. 11c–e). Such systematic variations are also

349   observed in other Stage 3 crystals (Fig. 12) that show a general covariation of the Sr

350   and O isotopic compositions with the contents of Nb, Ta, and Mo (by inference that

351   dark CL corresponds to Mo rich sections). Sections with high $\delta^{18}O$ values have

16

352   relatively low $^{87}Sr/^{86}Sr$ ratios and high Nb and Ta contents (mean 144 and 0.7 ppm,

353   respectively), whereas fluids with low $\delta^{18}O$ values have higher $^{87}Sr/^{86}Sr$ ratios and are

354   depleted in Nb and Ta concentration (mean 12 and 0.03 ppm, respectively) (Fig. 12).

355   The zoning may show repetition as late overgrowth may have similar Sr and O

356   isotopic compositions and Nb, Ta, and Mo contents as the core sections (Fig. 12).

357   **DISCUSSION**

358   **Temporal evolution of scheelite in the Fujiashan deposit**

359   The composition of skarn minerals reflects the inventory of the magmatic-

360   hydrothermal fluids, the consumed carbonate wall rocks, and the reaction history of

361   the fluids along their migration path (Romer et al. 2015; Xu et al. 2021). Scheelite

362   crystallizing during the reaction of the magmatic-hydrothermal fluids with the

363   carbonate wall rocks records some signatures that dominantly derive from the fluid

364   and some signatures that dominantly derive from the carbonates (Song et al. 2019; Li

365   et al. 2021a). For instance, the inventory of the ore elements W, Mo, Nb, and Ta is

366   mainly derived from the magmatic fluid. In contrast, the elements Ca, Mg, and Sr are

367   likely to be largely derived from the carbonates wall rocks, in part as the contents of

368   these elements are relatively low in highly evolved granites and magmatic fluids

369   (Poulin et al. 2018). The REE elements may have been introduced by the magmatic

370   fluid or originate from silicate impurities in the consumed carbonate wall rocks.

371   The presence of trace elements in scheelite not only reflects the availability of trace

372   elements in the fluid, but also the capacity of scheelite to incorporate these elements

17

373   in the sites occupied by Ca or W (Ghaderi et al. 1999; Brugger et al. 2000). Calcium

374   may be substituted in scheelite by Sr and other double-charged elements (e.g., Eu) and

375   to some extent by triple charged ions (e.g., REE), whereas W may be substituted by

376   highly charged ions, such as Mo, Nb, and Ta (Ghaderi et al. 1999; Poulin et al. 2016).

377   High contents of these elements in some scheelite crystals demonstrate that these

378   elements are compatible in the scheelite structure. Elements that are highly

379   compatible in scheelite may become depleted in the fluid during scheelite growth.

380   Thus, low contents of these elements provide evidence that these elements do not

381   have high contents in the fluid, but leaves open whether this fluid originally did not

382   have high contents of these elements or became depleted with time. In contrast, the

383   absence of elements that are not compatible in the scheelite lattice, such as single

384   charged ions (Li, Rb, Cs), but also small or large double charged ions (e.g., Be, Ba)

385   do not imply that these elements are not present in the fluid (Poulin et al. 2016).

386   The Sr isotope composition in scheelite is determined by the sources of Sr and

387   their isotopic compositions and may vary as the relative contribution of these sources

388   changes with development of the skarn system. Strontium sources include the granite,

389   the carbonates, whose Sr isotopic composition represents the Sr composition of

390   seawater at the time the carbonates precipitated, and detrital silicate impurities in the

391   carbonates that may have a continental source. The carbonates dominate the Sr budget

392   and are the major source of Sr as long as the carbonates are consumed during skarn

393   formation. Once early formed skarn minerals prevent further reaction of the

394   carbonates, the Sr isotopic composition will change as the silicate minerals (including

395   earlier formed skarn minerals) become important Sr sources (Heinrich et al. 1994;

396   Romer et al. 2005). Detrital silicate minerals in the carbonate wall rocks may have

397   higher $^{87}Sr/^{86}Sr$ ratios than carbonates and authigenic minerals of the Qixia group.

398   The broad ranges of trace element contents (Figs. 6 and 8) and Sr isotopic

399   compositions (Fig. 9) among scheelite of the four stages illustrate the following

400   general process of fluid-rock interaction: magmatic fluids emanating from the

401   granodiorite porphyry and migrating along the aquifer change their composition by

402   reaction with the carbonate wall rocks. Fluid-driven decarbonation of the carbonate

403   rocks adds Ca and Sr to the fluid and results in the precipitation of Ca-rich skarn

404   minerals. The formation of these minerals also changes the fluid composition, as the

405   minerals may scavenge a wide range of trace and ore elements from the fluid. Later

406   alteration of early formed skarn minerals may release early scavenged ore elements

407   and make them available for redistribution. Therefore, the composition of ore-forming

408   fluids from different stages does not only reflect the source, but is strongly affected by

409   fluid-driven reactions between aquifer and aquitard.

410   **Scheelite crystallization in open and closed systems**

411   Trace element contents of scheelite differ for crystallization in open and closed

412   systems (Brugger et al. 2000; Li et al. 2021a). In open systems, trace element contents

413   are controlled by availability from the fluid, reflecting both the source and the history

414   of trace element addition and loss along the path of fluid flow. Scheelite crystallizing

415   from such a system may show little variation. In closed systems, elements compatible

416   in scheelite become depleted in the fluid with time, resulting in systematic drops in

417   element contents from the core to the rim of crystals, as observed here for scheelite

418   with a Mo-rich core and a Mo-poor rim (Fig. 11).

419   A positive Eu anomaly is commonly thought to indicate that Eu^{2+} is enriched

420   relative to Eu^{3+}, reflecting relatively reduced conditions, whereas a negative Eu

421   anomaly is indicative of more oxidized conditions (e.g., Bau 1991). However,

422   changes in pH of the fluid, as during the release of CO_2 from carbonate rocks during

423   fluid-rock interaction and formation of skarn minerals, also may produce an Eu

424   anomaly at unchanged temperature and fO_2 (Brugger et al. 2008) as observed for

425   Sch1a and Sch1b (Figs. 7a, b). Similarly, the Mo content of scheelite is thought to

426   correlate positively with fO_2 (Hsu 1977). In fluid-dominated (i.e., open) systems,

427   these simplified relations may apply. In closed systems, however, the preferred

428   incorporation of Eu and Mo, reflected by a positive Eu anomaly and high Mo contents

429   of early crystallized scheelite, results in the depletion of Eu and Mo in the fluid. This

430   depletion in turn results in lower Eu anomalies and lower Mo contents in later

431   crystallized scheelite. With extreme depletion scheelite may have negative Eu

432   anomalies and very low Mo contents. The depletion in Mo is also reflected in a

433   change of fluorescence color from yellow to blue (Hsu and Galli 1973). Recurrent

434   influx of fluid, as known from systems that develop by a crack-and-seal mechanism

435   (e.g., Cathelineau et al. 2017), provides Eu and Mo and starts a new growth zone with

436   progressive Eu depletion (with a shift from a positive to a negative Eu anomaly) and

437   Mo depletion in Sch3a (Figs. 11c, d). Thus, in closed systems, variations in δEu and

438   Mo contents does not reflect the redox environment of mineral growth, but is likely to

20

439   represents a reservoir effect.

440   The contents of Mo, Nb, and Ta in the core of scheelite from Stage3 are high and

441   seem to carry only little (Figs. 11 and 12). During the growth of these scheelite cores,

442   the mineralizing system behaved like an open system, i.e., the high contents of these

443   trace elements seem to have been supported by high contents in the fluid that is

444   continuously replenished. For these segments of scheelite, δEu possibly reflects the

445   redox environment. The sudden drop of Mo, Nb, and Ta contents reflects the

446   transition from a system with continuous flow of magmatic fluids to a system with

447   restricted fluid flow, whereas the overgrowth zones with low Mo, Nb, and Ta contents

448   by zones with high Mo, Nb, and Ta contents reflects the transition from a system with

449   restricted magmatic fluid flow to a system with continuous magmatic fluid flow (Figs.

450   11 and 12).

451   **Pulsed flow of magmatic fluid during scheelite deposition**

452   The high contents of Mo, Nb, and Ta in scheelite (Figs. 6b, c) are signatures of the

453   magmatic fluid, as the contents of these elements are low in the carbonate wall rocks

454   and fluids originating from the wall rocks (Poulin et al. 2018; Li et al. 2022b).

455   Interaction between the magmatic fluid and the wall rocks or the mixing with another

456   fluid could reduce the contents of Mo, Nb, and Ta in the magmatic fluid, although not

457   by the several orders of magnitude that would be necessary to explain the contrasting

458   contents of Mo in the core and rims of scheelite (Fig. 8). Thus, the oscillatory

459   variation of the concentration of these elements in scheelite reflects the recurrent

460   changes from fluid flow in open veins to fluid trapped in closed veins, with

461 replenishment of magmatic fluid mirrored in the repeated increase of Mo, Nb, and Ta

462 contents (Figs. 8 and 12). Crystallization of scheelite, however, did not occur in a

463 strictly closed system as the Sr isotopic composition varies from core to rim (Fig. 9).

464 The large range in $^{87}Sr/^{86}Sr$ implies that consumption of the carbonate wall rocks (or

465 earlier formed skarn minerals), which have higher $^{87}Sr/^{86}Sr$ ratios than the original

466 magmatic fluid, contributed increasingly more Sr to the enclosed fluid (Fig. 9). The

467 increase in Sr contents and the variation of $^{87}Sr/^{86}Sr$ from the core to the rim of

468 scheelite implies that interaction between the magmatic fluid and carbonate rock

469 continued during the crystallization of scheelite. The Sr contents in marine carbonates

470 are expected to be much higher than those of a fluid emanating from a highly evolved

471 (Sr-poor) granite (Poulin et al. 2018). Therefore, minor contributions from the wall

472 rocks will have a significant effect on the $^{87}Sr/^{86}Sr$ ratios of the fluid.

473 Dissolution of wall rocks also changes the $\delta^{18}O$ of the fluid. Thus, the large

474 variations of $\delta^{18}O_{sch}$ (–10.5 ‰ to 7.7 ‰) and pulsed variation of $\delta^{18}O_{sch}$ at each stage

475 (Fig. 10a) not only reflects the fluid source, but also dissolution of wall rocks (both

476 carbonates and earlier formed calc-silicate minerals), possible fluid mixing and/or

477 phase separation, temperature dependent fractionation between scheelite and fluid,

478 and the precipitation history before scheelite precipitation. Calculation of $\delta^{18}O_{fluid}$

479 values using the scheelite data and the temperature of fluid inclusions yields a similar

480 curve as the one observed for $\delta^{18}O_{sch}$ values, but with a systematic shift toward lower

481 $\delta^{18}O_{fluid}$ values, as later scheelite crystalized at lower temperature (Fig. 10a, b). The

482 retrograde, quartz-sulfide, and carbonate stages formed at the temperature ranges of

22

483   400 to 350 ℃, 300 to 250 ℃, and 150 to 100 ℃, respectively (Lei et al. 2018). These

484   temperature ranges can account for a variation of $\delta^{18}O_{sch}$ in scheelite of 0.5 ‰, 0.8 ‰,

485   2.2 ‰, respectively, as shown in Appendix Figure A1. Thus, the observed within-

486   crystal variation of $\delta^{18}O_{sch}$ cannot be accounted for by different temperature alone.

487   Carbonate rocks commonly have high $\delta^{18}O$ values (Chacko et al. 2001). Thus,

488   dissolution of wall rocks increases the $\delta^{18}O$ of the ore-forming fluid. Similarly, the

489   loss of a vapor phase (cf. Lei et al. 2018) shift $\delta^{18}O$ of the remaining fluid to a higher

490    $\delta^{18}O$. Two processes that may shift $\delta^{18}O$ of the fluid to lower values are the

491   crystallization of skarn minerals (Heinrich et al. 2004, Heinrich 2007) and the mixing

492   with a meteoric fluid (Meinert et al. 2005). Crystallization of skarn minerals in a

493   closed system drives the fluid composition to lower $\delta^{18}O$ values and, therefore, makes

494   that later crystallized minerals have gradually lower $\delta^{18}O$ values (Figs. 10b and 13).

495   The very low $\delta^{18}O$ values of some Sch4b, however, may not be obtained by

496   crystallization of skarn minerals alone, but also reflect the influx of meteoric water to

497   the ore-forming system during the end of the carbonate stage, possibly due to the

498   transition from ductile to brittle deformation of the carbonate rocks at lower

499   temperature and/or pressure (Fournier. 1999; Sillitoe. 2010).

500   The contrasting Mo, Nb, Ta contents and Sr and O isotopic compositions in

501   scheelite primarily reflect recurrent changes from open to sealed veins with pulsed

502   addition of magmatic fluid during scheelite crystallization and some dissolution of the

503   wall rocks, which are dominated by carbonate minerals during early stages of skarn

504   formation and skarn minerals during later stages. In an open, fluid dominated system

505   the contents of Mo, Nb, and Ta in scheelite are high and the Sr and O isotopic

506   compositions of scheelite are dominated by the composition of the magmatic fluid.

507   Crystallization in a closed or restricted system, elements highly compatible in

508   scheelite become depleted and the formation of skarn minerals shifts $\delta^{18}O$ to lower

509   values. All these changes do not require the addition of a meteoric fluid, with the

510   possible explanation of late-stage scheelite with very low $\delta^{18}O$ values (as low as –

511   10.86 %; Fig. 13).

512   **IMPLICATIONS**

513   The source of ore-forming fluids is critical for the understanding of the genesis of

514   deposits. We present in-situ trace element and Sr and O isotope data of scheelite

515   crystals from the Fujiashan W skarn deposit. Sch3a that crystallized from a magmatic

516   fluid in an open (source-controlled) system is characterized by well-developed

517   oscillatory zonation pattern, high Mo, Nb, and Ta contents and high $\delta^{18}O_{sch}$ values.

518   The transition of scheelite crystallization in a system with continuous supply of

519   magmatic fluid to a system with restricted fluid flow is characterized by a drop in Mo,

520   Nb, and Ta contents, a systematic change form positive to negative Eu anomalies, and

521   a shift to lower $\delta^{18}O_{sch}$ values. The oscillatory zonation in scheelite indicates that there

522   may have been recurrent changes from continuous to restricted availability of

523   magmatic fluids. Most importantly, the observed chemical and isotopic changes do

524   not require the involvement of additional fluid sources, instead, they may be obtained

525   by pulsed flow of a magmatic fluid. Furthermore, our observations imply that

526   variations in Eu and Mo contents do not require the involvement of different fluids or

527   contrasting redox conditions. Our findings are broadly applicable to other skarns

528   deposit and are likely to provide an important alternative to traditional interpretations

529   of zoned mineral compositions in ore deposits.

541   **REFERENCE**

542   Ávila, J.N., Ireland, T.R., Holden, P., Lanc, P., Latimore, A., Schram, N., Foster, J.,

543   Williams, I.S., Loiselle, L., and Fu, B. (2020) High-Precision, High-accuracy

544   oxygen isotope measurements of zircon reference materials with the SHRIMP-SI.

545   Geostandards and Geoanalytical Research, 44, 85–102.

25

546   Bau, M. (1991) Rare-earth element mobility during hydrothermal and metamorphic

547   fluid-rock interaction and the significance of the oxidation state of europium.

548   Chemical Geology, 93, 219–230.

549   Brugger, J., Lahaye, Y., Costa, S., Lambert, D., and Bateman, R. (2000)

550   Inhomogeneous distribution of REE in scheelite and dynamics of Archaean

551   hydrothermal systems (Mt. Charlotte and Drysdale gold deposits, Western

552   Australia). Contributions to Mineralogy and Petrology, 139, 251–264.

553   Brugger, J., Etschmann, B., Pownceby, M., Liu, W.H., Grundler, P., and Brewe, D.

554   (2008) Oxidation state of europium in scheelite: Tracking fluid-rock interaction

555   in gold deposits. Chemical Geology, 257, 26–33.

556   Cathelineau, M., Myagkiy, A., Quesnel, B., Boiron, M.C., Gautier, P., Boulvais, P.,

557   Ulrich, M., Truche, L., Golfier, F., and Drouillet, M. (2017) Multistage crack

558   seal vein and hydrothermal Ni enrichment in serpentinized ultramafic rocks

559   (Koniambo massif, New Caledonia). Mineralium Deposita, 52, 945–960.

560   Chacko, T., Cole, D.R., and Horita, J. (2001) Equilibrium oxygen, hydrogen and

561   carbon isotope fractionation factors applicable to geologic systems. Reviews in

562   Mineralogy and Geochemistry, 43, 1–81.

563   Chang, Y.F., Liu, X.P., and Wu, Y.C. (1991) The copper-iron belt of the lower and

564   middle reaches of the Changjiang River, Geological Publishing House, Beijing,

565   1–234 (in Chinese with English abstract).

566   Chang, Z.S., Shu, Q.H., and Meinert, L.D. (2019) Skarn deposits of China. Society of

567   Economic Geologists, Special Publication, 22, 189–234.

568   Cui, X.J., Nabelek, P. I., and Liu, M. (2001) Heat and fluid flow in contact

569   metamorphic aureoles with layered and transient permeability, with application

570   to the Notch Peak aureole, Utah. Journal of Geophysical Research: Solid Earth,

571   106, 6477–6491.

572   D'Errico, M.E., Lackey, J.S., Surpless, B.E., Loewy, S.L., Wooden, J.L., Barnes, J.D.,

573   Strickland, A., and Valley, J.W. (2012) A detailed record of shallow

574   hydrothermal fluid flow in the Sierra Nevada magmatic arc from low-δ^{18}O skarn

575   garnets. Geology, 40, 763–766.

576   Einaudi, M.T., Meinert, L.D., and Newberry, R.J. (1981) Skarn deposits. Economic

577   Geology, 75, 317–391.

578   Fournier, R.O. (1999) Hydrothermal processes related to movement of fluid from

579   plastic into brittle rock in the magmatic-epithermal environment. Economic

580   Geology, 94, 1193−1211.

581   Ghaderi, M., Palin, J.M., Campbell, I.H., and Sylvester, P.J. (1999) Rare earth

582   element systematics in scheelite from hydrothermal gold deposits in the

583   Kalgoorlie-Norseman region, Western Australia. Economic Geology, 94, 423–

584   437.

585   Guillong, M., Hametner, K., Reusser, E., Wilson, S.A., and Günther, D. (2005)

586   Preliminary characteristics of new glass reference materials (GSA-1G, GSC-1G,

587   GSD-1G and GSE-1G) by laser ablation-inductively coupled plasma-mass

588   spectrometry using 193 nm, 213 nm and 266 nm wavelengths. Geostandards and

589   Geoanalytical Research, 29, 315–331.

590   Heinrich, W. (1994) Potassium-fluor-richterite in metacherts from the Bufa del Diente

591   contact-metamorphic aureole, NE-México. Mineralogy and Petrology, 50, 259–

592   270.

593   Heinrich, W., Churakov, S.S., and Gottschalk, M. (2004) Mineral-fluid equilibria in

594   the system $CaO–MgO–SiO_2–H_2O–CO_2–NaCl$ and the record of reactive fluid

595   flow in contact metamorphic aureoles. Contributions to Mineralogy and

596   Petrology, 148, 131–149.

597   Heinrich, W. (2007) Fluid immiscibility in metamorphic rocks. Reviews in

598   Mineralogy and Geochemistry, 65, 389–430.

599   Hsu, L.C., and Galli, P.E. (1973) Origin of the Scheelite-Powellite Series of Minerals.

600   Economic Geology, 68, 681–696.

601   Hsu, L.C. (1977) Effects of oxygen and sulfur fugacities on the scheelite-tungstenite

602   and powellite-molybdenite stability relations. Economic Geology, 72, 664–670.

603   Ji, Y.H., Xie, G.Q., Zhu, Q.Q., Sun, X.F., and Li, X.H. (2019) Influence of

604   carbonaceous strata on skarn tungsten deposits: A case study of Fujiashan

605   deposit in eastern Hubei Province. Mineral Deposits, 38, 917–934 (in Chinese

606   with English abstract).

607   Jochum, K.P., Weis, U., Stoll, B., Kuzmin, D., Yang, Q.C., Raczek, I., Jacob, D.E.,

608   Stracke, A., Birbaum, K., Frick, D.A., Gunther, D., and Enzweiler, J. (2011)

609   Determination of reference values for NIST SRM 610–617 glasses following

610   ISO guidelines. Geostandards and Geoanalytical Research, 35, 397–429.

611   Lefebvre, M.G., Romer, R.L., Glodny, J., and Roscher, M. (2019) Skarn formation

612   and tin enrichment during regional metamorphism: the Hämmerlein polymetallic

613   skarn deposit. Lithos, 348, 105171.

614   Lei, X.F., Duan, D.F., Jiang, S.Y., and Xiong, S.F. (2018) Ore-forming fluids and

615   isotopic (H-O-C-S-Pb) characteristics of the Fujiashan-Longjiaoshan skarn W-

616   Cu-(Mo) deposit in the Edong District of Hubei Province, China. Ore Geology

617   Reviews, 102, 386–405.

618   Li, C., Zhou, L.M., Zhao, Z., Zhang, Z.Y., Zhao, H., Li, X.W., and Qu, W.J. (2018)

619   In-situ Sr isotopic measurement of scheelite using fs-LA-MC-ICPMS. Journal of

620   Asian Earth Sciences, 160, 38–47.

621   Li, J.W., Vasconcelos, P.M., Zhou, M.F., Deng, X.D., Cohen, B., Bi, S.J., Zhao, X.F.,

622   and Selby, D. (2014) Longevity of magmatic–hydrothermal systems in the Daye

623   Cu–Fe–Au District, eastern China with implications for mineral exploration. Ore

624   Geology Reviews, 57, 375–392.

625   Li, W., Xie, G.Q., Cook, N.J. Mao, J.W., Li, C. Ciobanu, C.L., and Zhang, Z.Y.

626   (2021a) Tracking dynamic hydrothermal processes: Textures, in-situ Sr-Nd

627   isotopes, and trace-element analysis of scheelite from the Yangjiashan vein-type

628   W deposit, South China. American Mineralogist, 106, 1987–2002.

629   Li, W., Xie, G.Q., Mao, J.W., and Zhang, H.C. (2021b) Mineralogy, fluid inclusion

630   and isotope signatures: Implications for the genesis of the Early Paleozoic

631   Yangjiashan scheelite-quartz vein deposit, South China. Ore Geology Reviews,

632   134, 104136.

633   Li, Y., Allen, M.B., and Li, X.H. (2022a) Millennial pulses of ore formation and an

634   extra-high Tibetan Plateau. Geology, 50, 665–669.

635   Li, Y., Zhang, R.Q., He, S., Chiaradia, M., and Li, X.H. (2022b) Pulsed exsolution of

636   magmatic ore-forming fluids in tin-tungsten systems: a SIMS cassiterite oxygen

637   isotope record. Mineralium Deposita, 57(3), 343–352.

638   Liu, L.J., Zhou, T.F., Fu, B., Ireland, T.R., Zhang, D.Y., Liu, G.X., Yuan, F., Zha,

639   X.P., and White, N.C. (2023) Multiple fluid sources in skarn systems: Oxygen

640   isotopic evidence from the Haobugao Zn-Fe-Sn deposit in the southern Great

641   Xing'an Range, NE China. American Mineralogist. https://doi.org/10.2138/am-

642   2022-8523.

643   Liu, Q., Li, Y.J., Cai, H.A., Li, H.M., Zeng, X.H., Sun, X.F., Liu, D.Q., and Tan, J.

644   (2021) Diagenetic and metallogenic ages, and geological significance of the

645   Fujiashan skarn type (Cu-) W Deposit, southeastern Hubei Province. Bulletin of

646   Geological Science and Technology, 40, 210–222 (in Chinese with English

647   Abstract).

648   Liu, Y.S., Hu, Z.C., Gao, S., Günther, D., Xu, J., Gao, C.G., and Chen, H.H. (2008) In

649   situ analysis of major and trace elements of anhydrous minerals by LA-ICP-MS

650   without applying an internal standard. Chemical Geology, 257, 34–43.

651   Lu, H.Z., Liu, Y., Wang, C., Xu, Y., and Li, H. (2003) Mineralization and Fluid

652   Inclusion Study of the Shizhuyuan W-Sn-Bi-Mo-F Skarn Deposit, Hunan

653   Province, China. Economic Geology, 98(5), 955–974.

654   Mao, J.W., Xie, G.Q., Duan, C., Pirajno, F., Ishiyama, D., and Chen, Y.C. (2011) A

655   tectono-genetic model for porphyry–skarn–stratabound Cu–Au–Mo–Fe and

656   magnetite–apatite deposits along the Middle–Lower Yangtze River Valley,

657   Eastern China. Ore Geology Reviews, 43, 294–314.

658   Meinert, L.D., Dipple, G.M., and Nicolescu, S. (2005) World skarn deposits.

659   Economic Geology 100th Anniversary Volume, 299–336.

660   Milsch, H., Heinrich, W., and Dresen, G. (2003) Reaction-induced fluid flow in

661   synthetic quartz-bearing marbles. Contributions to Mineralogy and Petrology,

662   146, 286–296.

663   Miranda, A.C.R., Beaudoin, G., and Rottier, B. (2022) Scheelite chemistry from skarn

664   systems: implications for ore-forming processes and mineral exploration.

665   Mineralium Deposita, 57, 1469–1497.

666   Pan, Y.M., and Dong, P. (1999) The Lower Changjiang (Yangzi/Yangtze River)

667   metallogenic belt, east central China: intrusion- and wall rock-hosted Cu–Fe–Au,

668   Mo, Zn, Pb, Ag deposits. Ore Geology Reviews, 15, 177–242.

669   Poulin, R.S., McDonald, A.M., Kontak, D.J., and McClenaghan, M.B. (2016) On the

670   relationship between cathodoluminescence and the chemical composition of

671   scheelite from geologically diverse ore-deposit environments. The Canadian

672   Mineralogist, 54, 1147–1173.

673   Poulin, R.S., Kontak, D.J., McDonald, A., and McClenaghan, M.B. (2018) Assessing

674   scheelite as an ore-deposit discriminator using its trace-element and REE

675   chemistry. The Canadian Mineralogist, 56, 265–302.

676   Raimbault, L., Baumer, A., Dubru, M., Benkerrou, C., Croze, V., and Zahm, A. (1993)

677   REE fractionation between scheelite and apatite in hydrothermal conditions.

678   American Mineralogist, 78(11–12), 1275–1285.

679   Romer, R.L., Heinrich, W., Schröder-Smeibidl, B., Meixner, A., Fischer, C.O., and

680   Schulz, C. (2005) Elemental dispersion and stable isotope fractionation during

681   reactive fluid-flow and fluid immiscibility in the Bufa del Diente aureole, NE-

682   Mexico: evidence from radiographies and Li, B, Sr, Nd, and Pb isotope

683   systematics. Contributions to Mineralogy and Petrology, 149, 400–429.

684   Romer, R.L., and Kroner, U. (2015) Sediment and weathering control on the

685   distribution of Paleozoic magmatic tin–tungsten mineralization. Mineralium

686   Deposita, 50, 327–338.

687   Ryan-Davis, J., Lackey, J.S., Gevedon, M., Barnes, J.D., Lee, C.A., Kitajima, K., and

688   Valley, J.W. (2019) Andradite skarn garnet records of exceptionally low $\delta^{18}O$

689   values within an Early Cretaceous hydrothermal system, Sierra Nevada, CA.

690   Contributions to Mineralogy and Petrology, 174, 68.

691   Shu, Q.A., Chen, P.L., and Cheng, J.R. (1992) Geology of Fe-Cu Ore deposits in

692   Eastern Hubei Province. Press of Metallurgical Industry, Beijing, 1–510 (in

693   Chinese with English abstract).

694   Sillitoe, R.H. (2010) Porphyry Copper Systems*. Economic Geology, 105(1), 3–41.

695   Song, G.X., Cook, N.J., Li, G.M., Qin, K.Z., Ciobanu, C.L., Yang, Y.H., and Xu, Y.X.

696   (2019) Scheelite geochemistry in porphyry-skarn W-Mo systems: A case study

697   from the Gaojiabang Deposit, East China. Ore Geology Reviews, 113, 103084.

698   Sun, K.K., and Chen, B. (2017) Trace elements and Sr-Nd isotopes of scheelite:

699   Implications for the W-Cu-Mo polymetallic mineralization of the Shimensi

700   deposit, South China. American Mineralogist, 102, 1114–1128.

701   Sun, K.K., Chen, B., and Deng, J. (2019) Ore genesis of the Zhuxi supergiant W-Cu

702   skarn polymetallic deposit, South China: Evidence from scheelite geochemistry.

703   Ore Geology Reviews, 107, 14-29.

704   Sun, S.S. McDonough, W.S. (1989) Chemical and isotopic systematics of oceanic

705   basalts: implications for mantle composition and processes. Geological Society,

706   London, Special Publications 42, 313–345.

707   Taylor, B.E., and O'Neil, J.R. (1977) Stable isotope studies of metasomatic Ca-Fe-Al-

708   Si skarns and associated metamorphic and igneous rocks, Osgood Mountains,

709   Nevada. Contributions to Mineralogy and Petrology, 63(1), 1–49.

710   Wesolowski, D., and Ohmoto, H. (1986) Calculated oxygen isotope fractionation

711   factors between water and the minerals scheelite and powellite. Economic

712   Geology, 81, 471–477.

713   Xie, G.Q., Mao, J.W., Li, X.W., Duan, C., and Yao, L. (2011) Late Mesozoic bimodal

714   volcanic rocks in the Jinniu basin, Middle–Lower Yangtze River Belt (YRB),

715   East China: Age, petrogenesis and tectonic implications. Lithos, 127, 144–164.

716   Xu, R., Romer, R.L., and Glodny, J. (2021) External fluids cause alteration and metal

717   redistribution in the granite-hosted Tangziwa Sn-Cu deposit, Gejiu district,

718   China. Lithos, 382–383, 105937.

719   Zhai, Y.S., Xiong, Y.L., Yao, S.Z., and Lin, X.D. (1996) Metallogeny of copper and

720   iron deposits in the Eastern Yangtse Craton, east-central China. Ore Geology

721   Reviews, 11, 229–248.

722   Zhang, L.G. (1985) Application of stable isotope in geosciences, Science and

723   Technology Publishing House, Shanxi, 1–267 (in Chinese).

724   Zhou, T.F., Wang, S.W., Fan, Y., Yuan, F., Zhang, D.Y., and White, N.C. (2015) A

725   review of the intracontinental porphyry deposits in the Middle-Lower Yangtze

726   River Valley metallogenic belt, eastern China: Ore Geology Reviews, 65, 433–

727   456.

728   Zhou, T.F., Nie, L.Q., Wang, S.W., Wang, F.Y., and Zhang, Q.M. (2019). Tungsten

729   deposits in the Middle-Lower Yangtze Metallogenic Belt, China. Acta

730   Petrologica Sinica, 35, 3592–3608 (in Chinese with English abstract).

731

732   FIGURE CAPTIONS

733 FIGURE 1. (a) Map showing the location of the Middle-Lower Yangtze River

734   metallogenic belt in China. (b) Map showing the distribution of major deposits and

735   related granitoids in the Middle-Lower Yangtze River metallogenic belt (modified

736   after Mao et al. 2011; Zhou et al. 2019). (c) Geological map of the Edong ore district

737   showing the main types of mineral deposits and intrusions (modified after Shu et al.

738   1992; Xie et al. 2011). TLF = Tancheng-Lujiang fault, XGF = Xiangfan-Guangji fault,

739   YCF = Yangxin-Changzhou fault.

740 FIGURE 2. (a) Geological map of the Fujiashan W deposit in southeastern Hubei

741   Province (modified after map from No. 1 Geological Party of Hubei Geological

742   Bureau). (b) Representative cross section from the eastern ore segment of the

743   Fujiashan W skarn deposit (modified after map from No. 1 Geological Party of Hubei

744   Geological Bureau).

745 **FIGURE 3.** Skarn zoning of drill hole at Fujiashan. (**a**) Fujiashan granodiorite porphyry.

746   (**b**) Photomicrograph of the Fujiashan granodiorite porphyry. (**c**) Orange garnet skarn

747   crosscutting or replacing dark brown garnet skarn. (**d**) Disseminated scheelite as

748   isolated inclusions within garnet. (**e**) Light brown garnet replaced by calcite and

749   pyrite. (**f**) Garnet replaced by pyroxene. (**g**) Distal red to dark green garnet skarn. (**h**)

750   Scheelite concentration along zones of garnet growth. (**i**) Light orange garnet skarn

751   crosscutting limestone. (**j**) Scheelite coexisting with molybdenite and pyrite at the

752   contact between garnet skarn and limestone. Abbreviation: Ap = apatite; Bi = biotite;

753   Cal = calcite; Ep = epidote; Grt = garnet; Kfs = K-feldspar; Mo = molybdenite; Pl =

754   plagioclase; Py = pyrite; Pyx = pyroxene; Qtz = quartz; Sch = scheelite.

755 **FIGURE 4.** Photographs showing the types of W mineralization in the Fujiashan deposit.

756   (**a**) Quartz-scheelite-pyrite vein cutting the garnet skarn. (**b**) Blue and yellow

757   fluorescence of individual scheelite crystals coexisting with pyrite and quartz. (**c**)

758   Garnet skarn with disperse scheelite, quartz and pyrite. (**d**) Calcite-scheelite veins

759   cutting garnet skarn. (**e**) Garnet skarn replaced by calcite and epidote. (**f**) Pyrite-

760   epidote vein cutting garnet skarn. (**g**) Quartz vein cutting garnet skarn. (**h**) Garnet

761   skarn with pyrite and chalcopyrite. (**i**) Molybdenite replacing garnet. (**j**) Quartz vein

762   with apatite, epidote and pyroxene. (**k**) Chlorite and epidote replaced by calcite. (**l**)

763   Scheelite and actinolite replaced by calcite. (**m**) Scheelite coexisting with pyrite in the

764   quartz vein. (**n**) Scheelite coexisting with chalcopyrite. (**o**) Coarse-grained scheelite in

35

765   calcite. Abbreviation: Act = actinolite; Ap = apatite; Cal = calcite; Ccp = chalcopyrite;

766   Ep = epidote; Fl = fluorite; Grt = garnet; Mo = molybdenite; Py = pyrite; Qtz =

767   quartz; Sch = scheelite; Ttn = titanite.

768 **FIGURE 5.** Cathodoluminescence (CL) images showing scheelite textures. (**a**) Subhedral,

769   homogeneous Sch1a and (**b**) subhedral, oscillatory zoned Sch1b from skarn stage 1.

770   (**c-d**) Oscillatory zoned Sch2a and Sch2b from the retrograde stage showing the

771   replacement of Sch2a by Sch2b. There are two modes of occurrence of Stage 3

772   scheelite, i.e., in the name giving quartz-sulfide stage and in high-grade W

773   mineralization. Scheelite from the quartz-sulfide stage (Sch3a) shows (**e-f**) irregular

774   oscillatory to patchy zoning with a Mo-rich core in euhedral crystals, whereas

775   scheelite from high-grade W mineralization (Sch3b) (**g**) typically is subhedral and has

776   relatively homogeneous CL response. Scheelite from the calcite stage shows (**h-i**)

777   well-developed oscillatory zoning in Sch4a with local irregular replacement by

778   Sch4b.

779 **FIGURE 6.** Trace element contents of different scheelite types. (**a**) Sr, (**b**) Mo, (**c**) Nb+Ta,

780   and (**d**) total REE contents have been determined by LA-ICP-MS. The trendlines

781   connecting the averages of each group are for orientation only. Data from Appendix

782   Table S2.

783 **FIGURE 7.** Chondrite-normalized REE fractionation patterns of scheelite from the

784   Fujiashan deposit. Normalization values were taken from Sun and McDonough

785   (1989).

786 **FIGURE 8.** Cathodoluminescence and LA-ICP-MS element maps of representative Sch3a

787   crystal, showing the distribution of trace elements (ppm).

788 FIGURE 9. Variations of the Sr isotopic composition of different scheelite types. Note, the

789     $^{87}Sr/^{86}Sr$ ratios of each type fall in relatively broad ranges that overlap and generally

790   fall between the compositions of the granodiorites and the sedimentary rocks of the

791   wall rocks.

792 FIGURE 10. $\delta^{18}O_{Sch}$ and $\delta^{18}O_{fluid}$ values for Fujiashan deposit sorted by different stage

793   scheelite generations. (a) In-situ O isotope data of scheelite with 2SD error bars. (b)

794   Calculated $\delta^{18}O$ values of the hydrothermal fluids based on the measured $\delta^{18}O$ values

795   of scheelite (Meteoric water is from Zhang, 1985). Note, the overall $\delta^{18}O_{fluid}$ values

796   show pulsed variation from early to late stages.

797 FIGURE 11. Geochemistry and in-situ Sr-O isotope data of Sch3a. (a) Red and blue

798   symbols represent position of in-situ LA-ICP-MS trace element contents, Sr isotope

799   compositions, respectively. (b) Nb content of scheelite. (c) δEu value of scheelite. (d)

800   Mo content of scheelite. (e) In-situ Sr isotope data of scheelite with 2SE error bars.

801 FIGURE 12. Compositional zoning of Sch3a. (a) CL image with sampling spots (red, blue

802   and green symbols) for in-situ LA-ICP-MS trace element analysis (red symbols) and

803   Sr (blue symbols) and O isotope analysis (green symbols). (b) Nb and (c) Ta contents.

804   (d) In-situ Sr isotope analyses with 2SE error bars. (e) In-situ O isotope analyses with

805   2SD error bars.

806 FIGURE 13. (a) CL image of Sch4a and Sch4b with spots for in-situ O isotope analysis.

807   (b) In-situ O isotope spot of scheelite.

808   SUPPLEMENTARY MATERIAL

37

809   **Supplementary**[1]

810   **TABLE S1.** Description of samples discussed in the present study

811   **TABLE S2.** Laser ablation inductively coupled plasma mass spectrometry trace

812   element data and average minimum detection limits for scheelite from the Fujiashan

813   deposit (ppm)

814   **TABLE S3.** Complete *in-situ* Sr isotope dataset for scheelite from the Fujiashan

815   deposit

816   **TABLE S4.** Complete *in-situ* O isotope dataset for scheelite from the Fujiashan deposit

817   **FIGURE A1.** Oxygen isotope fractionation between scheelite and water as a function

818   of temperature.

Table 1. LA-ICP-MS data for scheelite (Stage1 and Stage2) from the Fujiashan deposit, eastern China (all contents in ppm)

Stage	1						2					
Sub-type	Sch1a (n=11)			Sch1b (n=11)			Sch2a (n=11)			Sch2b (n=5)		
	min	mean	max	min	mean	max	min	mean	max	min	mean	max
Na	20.2	28.5	52.3	20.6	53.8	118	13.5	33.9	121	13.6	29.9	38.3
Sr	99.6	141	161	103	159	184	183	217	272	141	181	247
Mo	4990	36000	49300	10600	18700	24700	21100	38900	69300	2640	10900	22100
Re	0.77	0.96	1.08	0.14	0.24	0.30	0.44	0.54	0.62	0.48	0.54	0.61
Nb	11.4	93.7	178	2.21	4.47	8.68	10.6	38.9	97.4	9.44	13.0	16.3
Ta	0.01	0.10	0.18	0.04	0.11	0.19	0.03	0.19	0.50	0.02	0.03	0.04
U	0.01	1.43	4.16	bdl	0.07	0.44	0.01	0.07	0.18	0.01	0.02	0.02
Pb	0.94	1.18	1.43	1.00	1.90	3.07	1.63	2.15	2.70	2.23	2.51	2.76
La	17.1	89.0	170	3.13	35.8	51.5	21.8	52.8	128	2.44	14.9	25.5
Ce	46.0	237	442	7.76	55.8	80.9	59.6	106	201	10.2	43.9	76.2
Pr	3.76	27.3	51.0	0.83	3.02	4.26	5.01	12.1	20.1	2.13	7.30	13.2
Nd	8.81	103	210	5.37	7.29	9.41	13.5	50.0	99.9	12.8	42.2	77.4
Sm	0.42	14.6	29.9	0.55	1.29	2.79	1.13	8.99	20.1	3.55	9.65	17.3
Eu	0.24	8.05	16.4	0.04	0.53	1.35	0.60	4.71	15.8	0.91	3.25	6.45
Gd	0.28	8.97	19.1	0.28	1.02	1.89	0.87	6.98	15.5	2.29	8.15	14.5
Tb	0.02	1.22	2.69	0.02	0.13	0.32	0.08	0.85	1.88	0.26	0.85	1.48
Dy	0.10	6.68	14.4	0.02	0.49	1.06	0.52	4.30	9.57	1.22	4.13	7.21
Ho	0.02	1.31	2.96	bdl	0.07	0.20	0.08	0.80	1.84	0.19	0.72	1.26
Er	0.03	3.38	7.51	0.02	0.17	0.46	0.17	1.87	4.44	0.38	1.49	2.73
Tm	bdl	0.43	1.02	bdl	0.01	0.03	0.02	0.19	0.51	0.04	0.16	0.28
Yb	0.01	2.56	6.30	0.01	0.06	0.16	0.08	0.80	2.20	0.17	0.70	1.22
Lu	bdl	0.34	0.88	bdl	0.01	0.01	0.01	0.07	0.27	0.02	0.07	0.13

Y	0.32	25.7	56.3	0.16	1.27	2.44	2.34	18.4	41.8	4.65	16.4	29.6
LREE	76.4	479	890	20.1	104	149	116	234	424	32.9	121	213
HREE	0.49	24.9	54.8	0.51	1.93	3.66	2.20	15.8	35.9	4.63	16.3	28.7
LREE/HREE	14.9	40.8	154	6.90	88.8	249	8.04	27.1	62.3	5.23	8.43	16.6
Total REE	76.9	504	945	23.0	105	153	119	250	438	39.1	137	242
Nb+Ta	11.4	93.8	178	2.33	4.57	8.72	10.8	39.1	97.7	10.5	13.2	16.3
δEu	1.65	2.09	2.43	0.29	0.90	1.83	0.67	1.96	4.21	0.92	1.16	1.52
δCe	1.11	1.22	1.41	1.18	1.33	1.39	0.98	1.06	1.13	1.02	1.05	1.09

Note: bdl = below detection limits.

Table 2. LA-ICP-MS data for scheelite (Stage3 and Stage4) from the Fujiashan deposit, eastern China (all contents in ppm)

Stage	3						4					
Sub-type	Sch3a (n=19)			Sch3b (n=13)			Sch4a (n=12)			Sch4b (n=5)		
	min	mean	max	min	mean	max	min	mean	max	min	mean	max
Na	16.5	53.4	171	0.09	25.0	49.7	8.54	19.8	33.5	12.4	15.2	18.3
Sr	84.9	152	281	150	169	223	150	182	215	308	382	441
Mo	2010	6780	21700	3780	4310	4890	7110	10600	17300	844	1130	1640
Re	0.45	0.55	0.70	0.42	2.07	3.91	0.29	0.33	0.37	0.16	0.23	0.31
Nb	2.81	36.7	156	0.88	6.75	15.1	1.19	3.06	6.31	0.68	0.74	0.81
Ta	0.02	0.21	0.92	0.02	0.03	0.05	0.02	0.12	0.87	bdl	bdl	bdl
U	bdl	0.22	0.81	bdl	0.02	0.07	0.01	0.02	0.04	0.11	0.21	0.26
Pb	0.86	3.00	7.35	2.14	2.89	5.13	1.58	1.90	2.52	0.46	1.17	1.79
La	9.32	36.2	73.9	8.30	12.2	18.8	13.2	14.9	16.9	16.2	19.5	22.6
Ce	30.5	143	308	20.4	47.9	87.4	29.9	38.1	51.8	18.9	25.1	38.2
Pr	4.48	24.5	62.2	1.98	7.96	16.7	2.48	3.47	5.58	1.29	1.93	3.43
Nd	14.7	123	359	5.55	42.7	96.1	4.84	8.03	12.5	4.28	7.58	16.0
Sm	1.08	28.9	89.6	1.34	9.79	22.1	0.22	0.55	1.42	0.52	1.22	2.57
Eu	0.33	17.0	34.1	0.03	3.01	6.82	0.09	0.31	1.18	0.54	0.94	1.53
Gd	0.46	23.5	72.7	1.56	9.08	19.3	0.18	0.39	1.16	0.42	0.83	1.07
Tb	0.04	3.61	12.8	0.18	1.12	2.42	0.02	0.04	0.11	0.09	0.13	0.22
Dy	0.28	22.0	83.2	1.00	6.06	13.0	0.05	0.20	0.68	0.49	0.70	0.89
Ho	0.02	4.30	16.8	0.18	1.25	2.59	0.02	0.03	0.13	0.08	0.14	0.20
Er	0.07	11.0	46.7	0.37	3.07	6.67	0.03	0.08	0.29	0.32	0.42	0.57
Tm	0.02	1.29	6.72	0.03	0.32	0.70	bdl	0.01	0.02	0.04	0.06	0.10
Yb	0.09	6.17	39.7	0.11	1.39	3.05	bdl	0.04	0.18	0.38	0.43	0.47
Lu	0.02	0.63	4.89	0.01	0.13	0.29	bdl	0.00	0.01	0.05	0.06	0.07

Y	1.46	99.1	342	5.78	33.7	71.7	0.54	0.95	2.54	4.87	7.42	13.4
LREE	74.3	372	910	38.1	123.5	248	52.8	65.3	86.3	46.3	56.3	77.9
HREE	0.96	72.5	281	3.52	22.4	48.0	0.32	0.79	2.58	1.97	2.78	3.34
LREE/HREE	2.54	14.3	77.3	4.29	8.06	15.5	22.2	110	175	16.6	20.4	23.5
Total REE	75.3	445	1103	41.9	146	296	53.7	66.1	87.0	48.3	59.1	81.3
Nb+Ta	4.70	22.4	77.3	0.90	6.78	15.1	1.22	3.18	6.38	0.68	0.74	0.81
δEu	1.09	2.94	11.9	0.05	0.61	1.16	0.95	1.82	3.08	2.54	2.97	3.56
δCe	1.03	1.18	1.34	1.18	1.27	1.42	1.21	1.30	1.42	0.90	1.01	1.26

Note: bdl = below detection limit.

Table 3. In situ Sr-O isotope data for scheelite from the Fujiashan deposit, Eastern China

Stage	Sub-type			^{85}Rb[V]	^{88}Sr[V]	^{87}Rb/^{86}Sr	2SE	^{87}Sr/^{86}Sr	2SE	δ^{18}O	2SD
1	Sch1a	min		0.00002	0.85844	0.00007	0.00005	0.70682	0.00022	4.72	0.60
	Sch1a	mean	Sr: n=5, O: n=12	0.00009	1.15933	0.00032	0.00006	0.70739	0.00029	5.64	0.61
	Sch1a	max		0.00018	1.36499	0.00073	0.00010	0.70770	0.00044	6.01	0.63
	Sch1b	min		0.00000	0.80191	0.00003	0.00007	0.70706	0.00028	3.46	0.60
	Sch1b	mean	Sr: n=4, O: n=8	0.00014	0.91325	0.00060	0.00014	0.70748	0.00034	4.22	0.61
	Sch1b	max		0.00041	1.12536	0.00161	0.00026	0.70811	0.00040	4.81	0.66
2	Sch2a	min		0.00001	0.89178	0.00005	0.00003	0.70663	0.00019	4.59	0.60
	Sch2a	mean	Sr: n=5, O: n=12	0.00015	1.26652	0.00037	0.00008	0.70705	0.00026	5.71	0.60
	Sch2a	max		0.00063	1.88203	0.00146	0.00014	0.70735	0.00033	6.53	0.61
	Sch2b	min		0.00004	1.04767	0.00004	0.00001	0.70749	0.00007	2.98	0.60
	Sch2b	mean	Sr: n=4, O: n=9	0.00018	5.44199	0.00010	0.00003	0.70758	0.00013	3.90	0.60
	Sch2b	max		0.00054	14.55488	0.00022	0.00007	0.70772	0.00027	4.87	0.62
3	Sch3a	min		0.00005	1.11017	0.00007	0.00003	0.70661	0.00015	1.89	0.60
	Sch3a	mean	Sr: n=9, O: n=19	0.00035	1.79358	0.00068	0.00008	0.70726	0.00021	3.92	0.60
	Sch3a	max		0.00104	2.37460	0.00236	0.00022	0.70804	0.00029	5.90	0.64
	Sch3b	min		0.00000	0.82684	0.00014	0.00008	0.70697	0.00027	3.96	0.60
	Sch3b	mean	Sr: n=6, O: n=25	0.00023	0.89860	0.00046	0.00013	0.70706	0.00034	5.18	0.60
	Sch3b	max		0.00096	1.11581	0.00261	0.00036	0.70720	0.00040	7.66	0.61
4	Sch4a	min		0.00008	1.21703	0.00015	0.00004	0.70616	0.00016	0.18	0.60
	Sch4a	mean	Sr: n=9, O: n=17	0.00041	1.68881	0.00091	0.00024	0.70730	0.00022	3.57	0.63
	Sch4a	max		0.00229	2.06418	0.00536	0.00168	0.70782	0.00048	5.23	0.66
	Sch4b	min		0.00012	1.76810	0.00023	0.00005	0.70853	0.00018	-10.52	0.66
	Sch4b	mean	Sr: n=3, O: n=6	0.00021	1.82506	0.00038	0.00005	0.70855	0.00020	-9.41	0.68

Sch4b	max		0.00029	1.86332	0.00051	0.00005	0.70855	0.00022	-8.71	0.70

Signal intensity is proportional to the contents of corresponding mass. A reading of 1 V corresponds to a current of $\sim 9.0 * 10^5$ cps.

Reported $^{87}Sr/^{86}Sr$ ratios correspond to measured ratios and have not been corrected for in situ growth of ^{87}Sr, which for an age of 150 Ma and a $^{87}Rb/^{86}Sr$ of 0.006 (the highest ratio obtained for the here analyzed scheelite samples results in a reduction of the $^{87}Sr/^{86}Sr$ ratio less than 0.00002, which is less than analytical uncertainty.
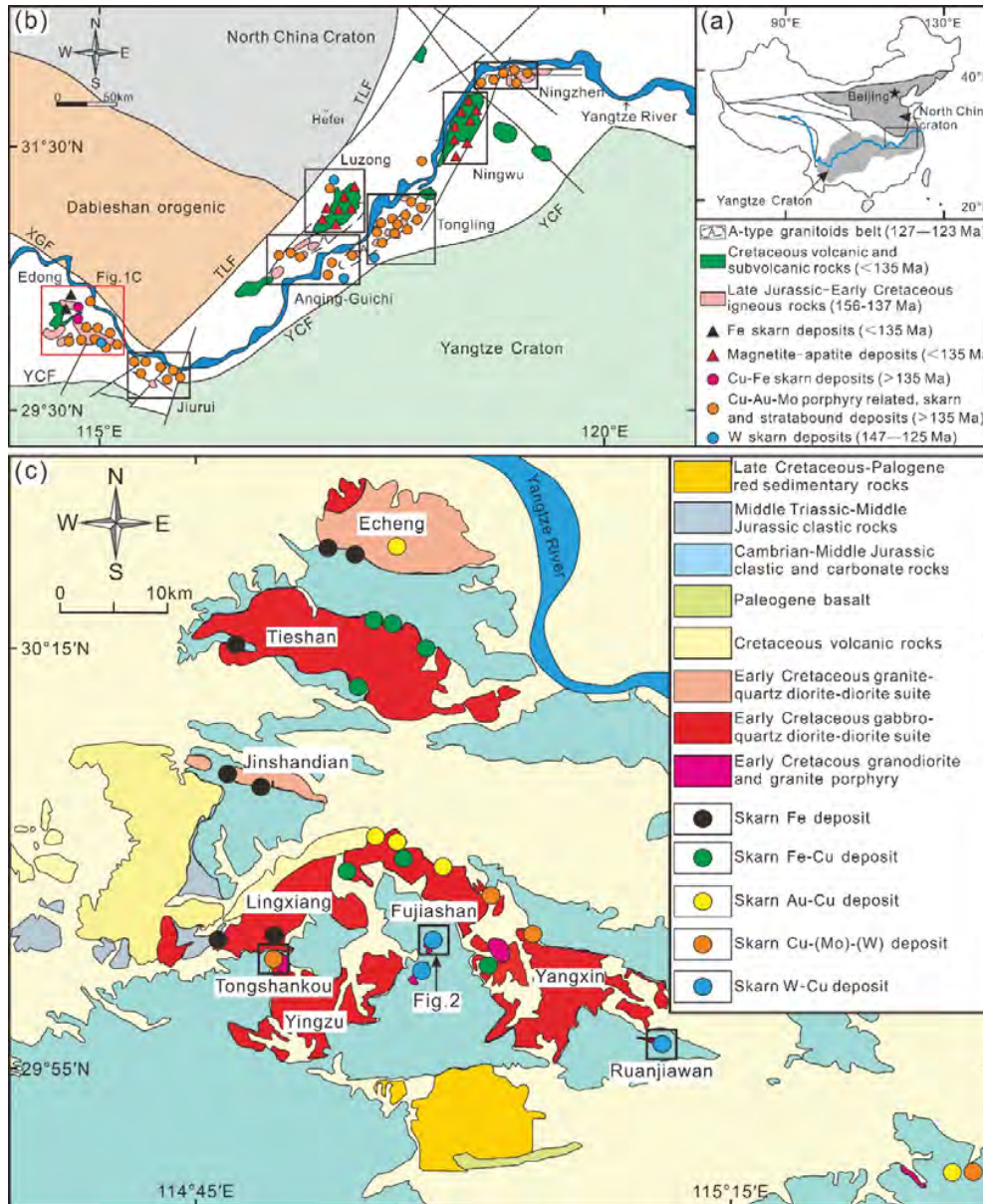
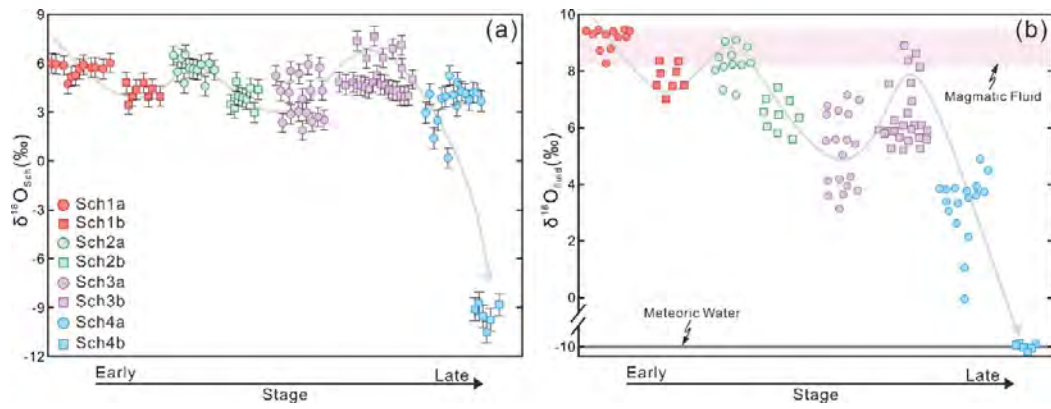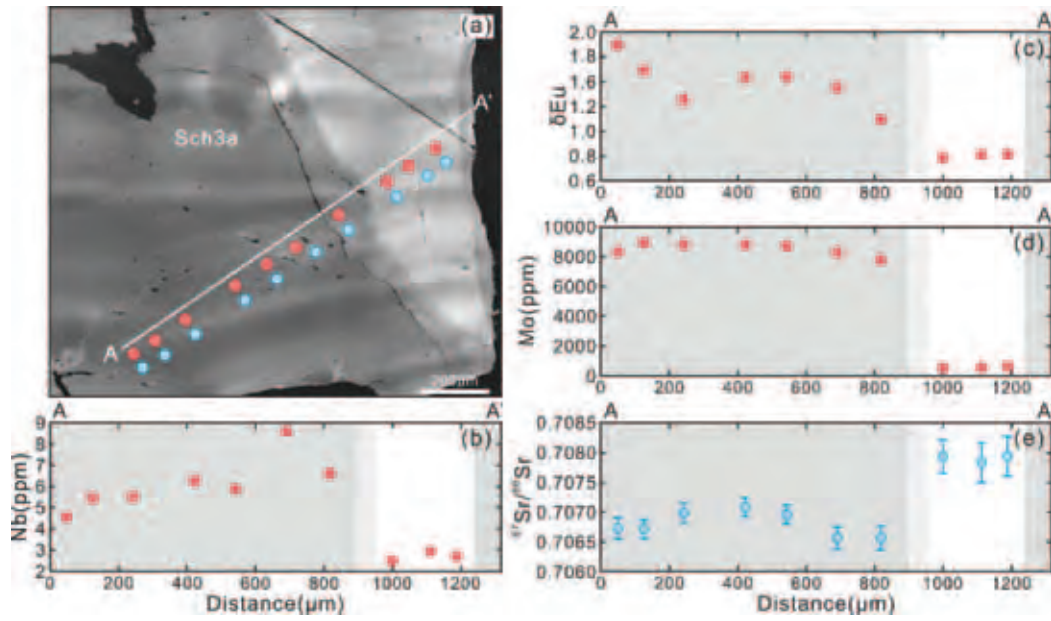Figure 1
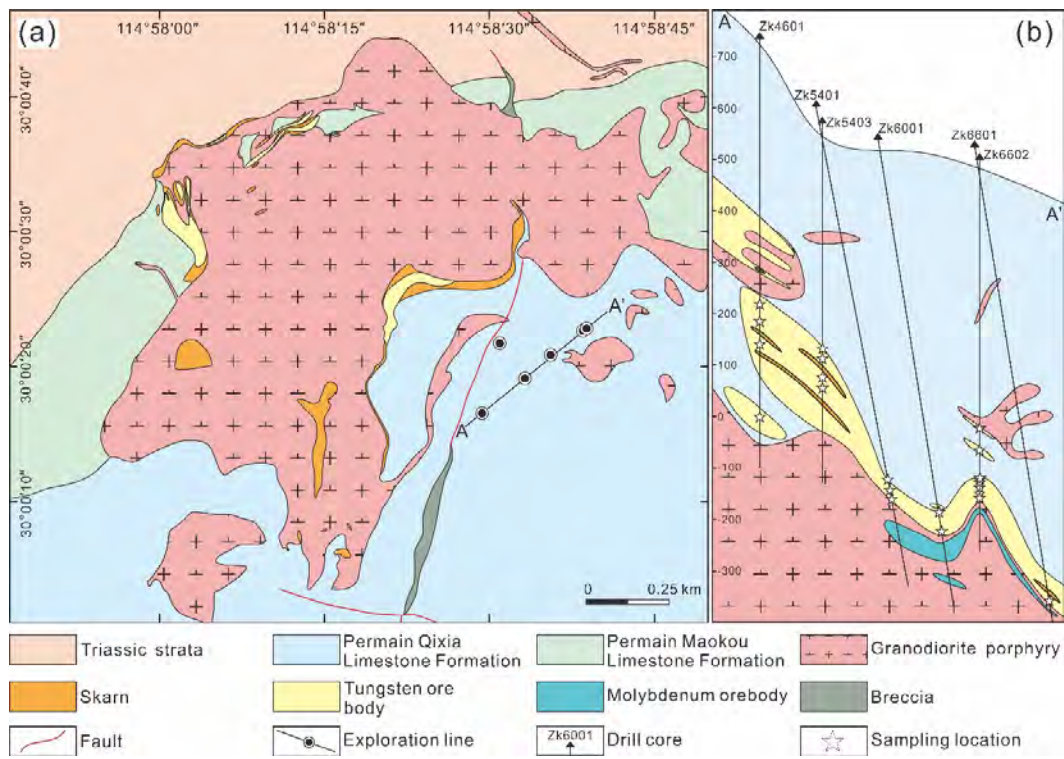
Figure 2
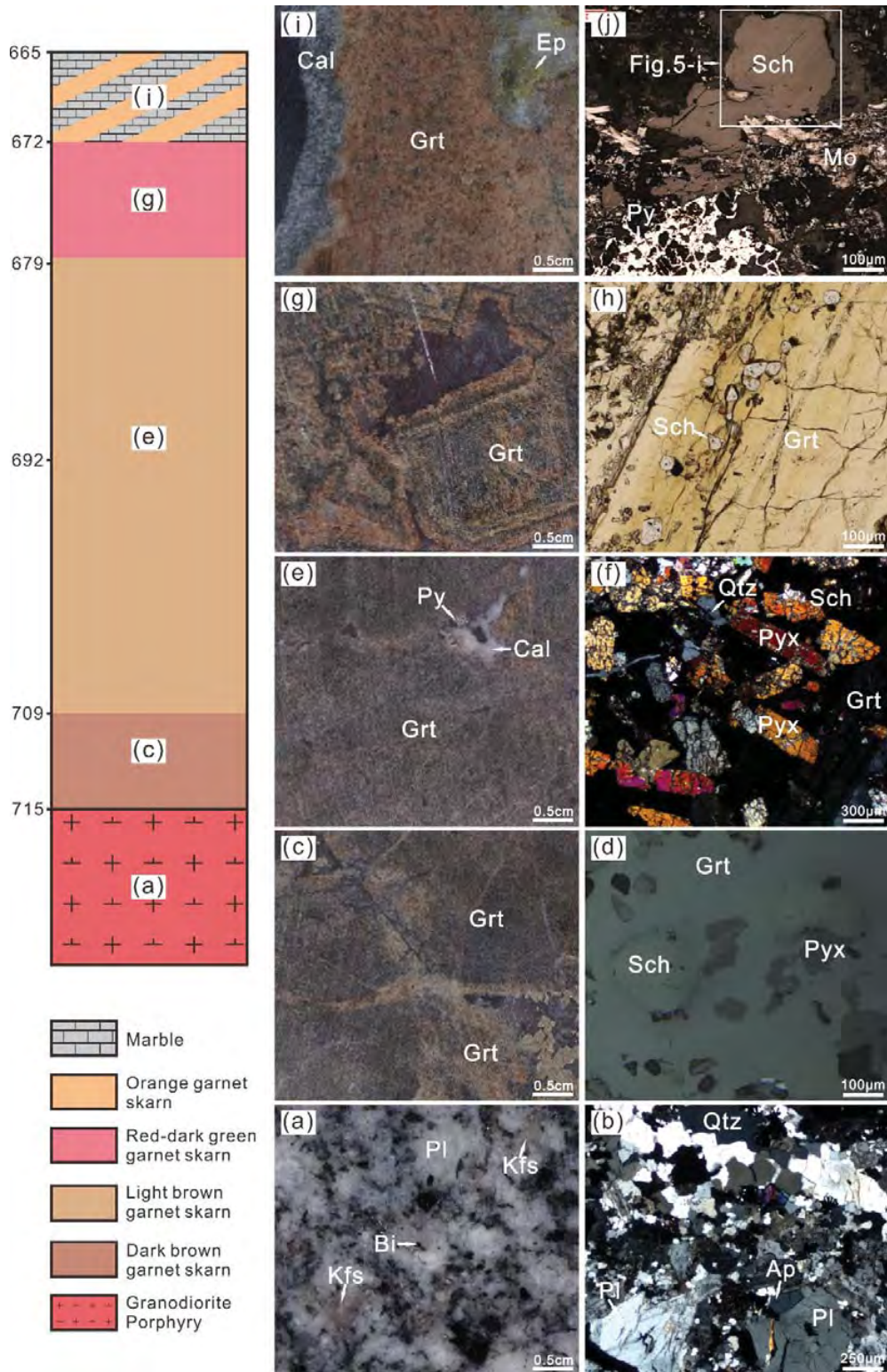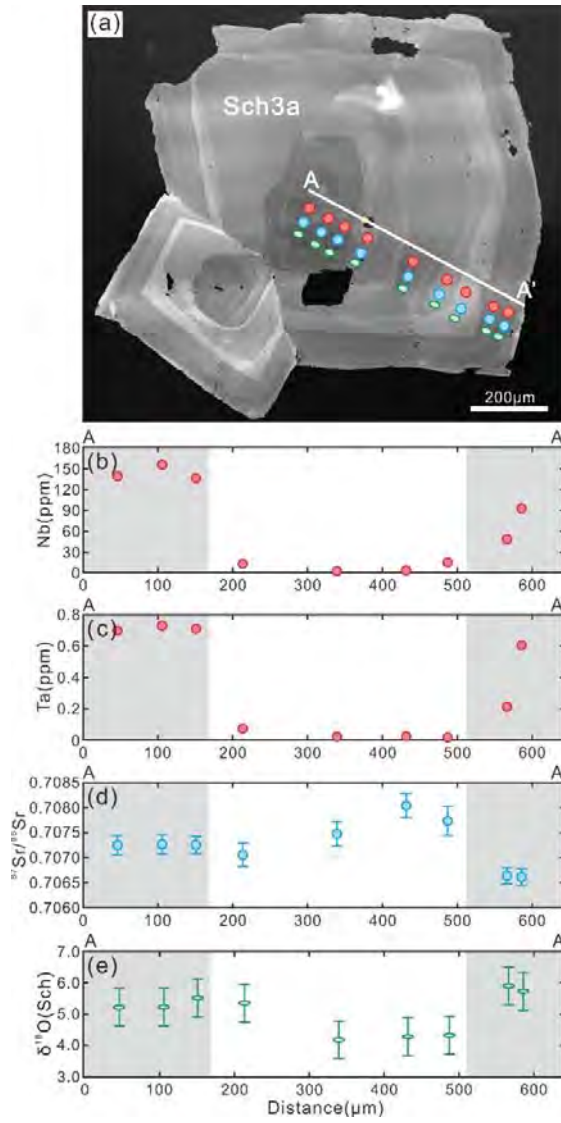
Figure 3
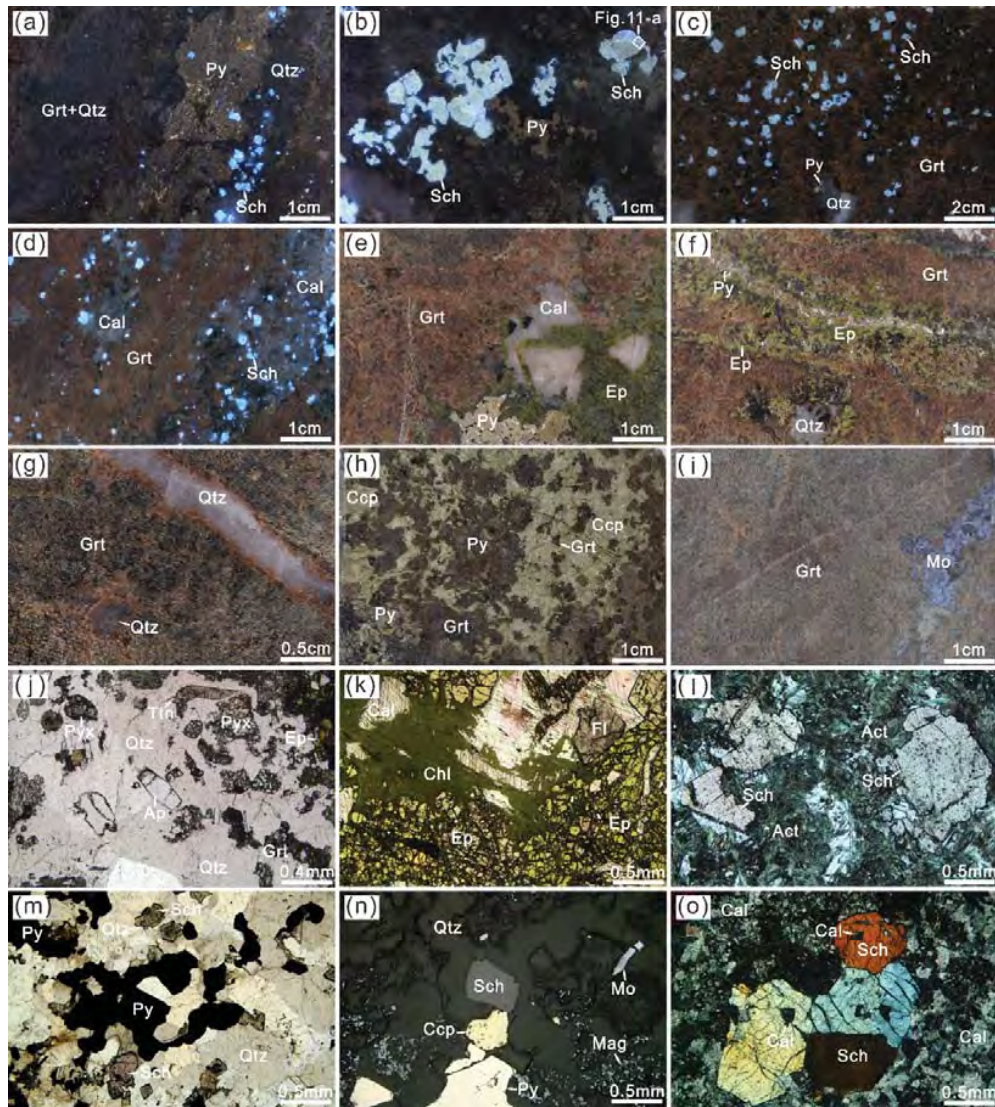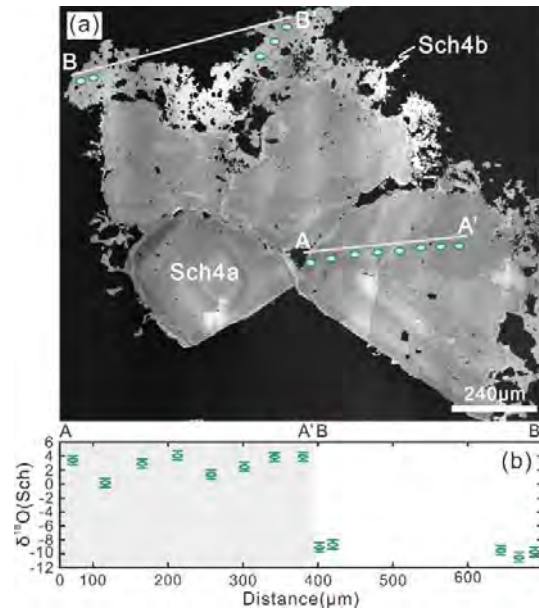
Figure 4
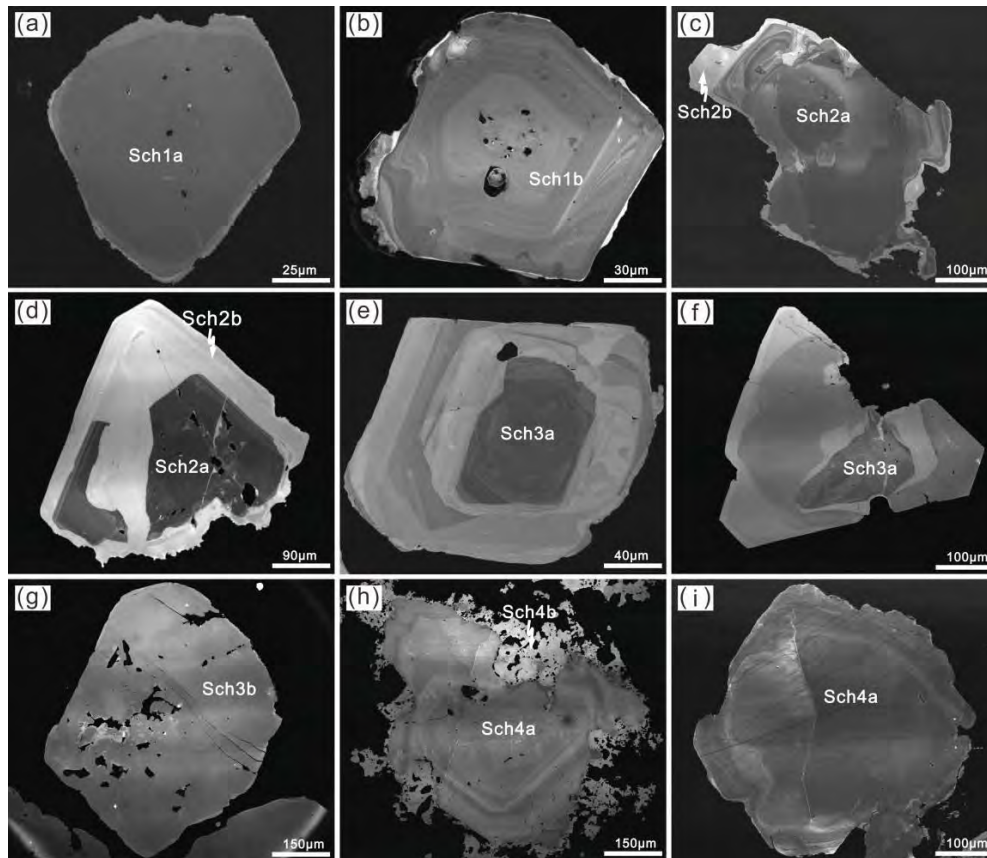
Figure 5
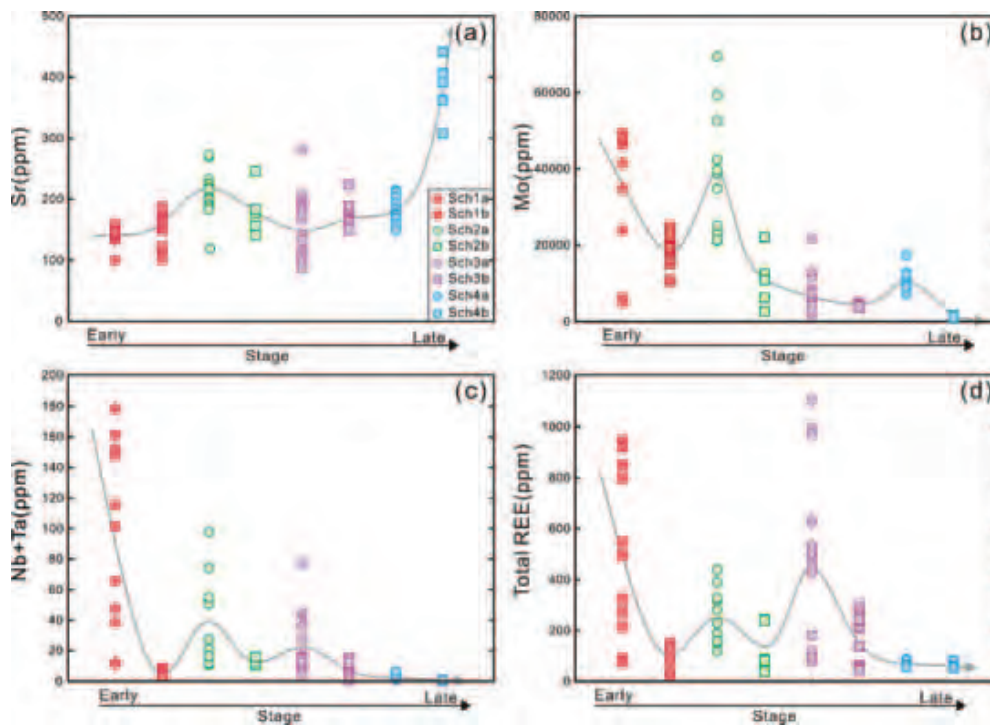
Figure 6
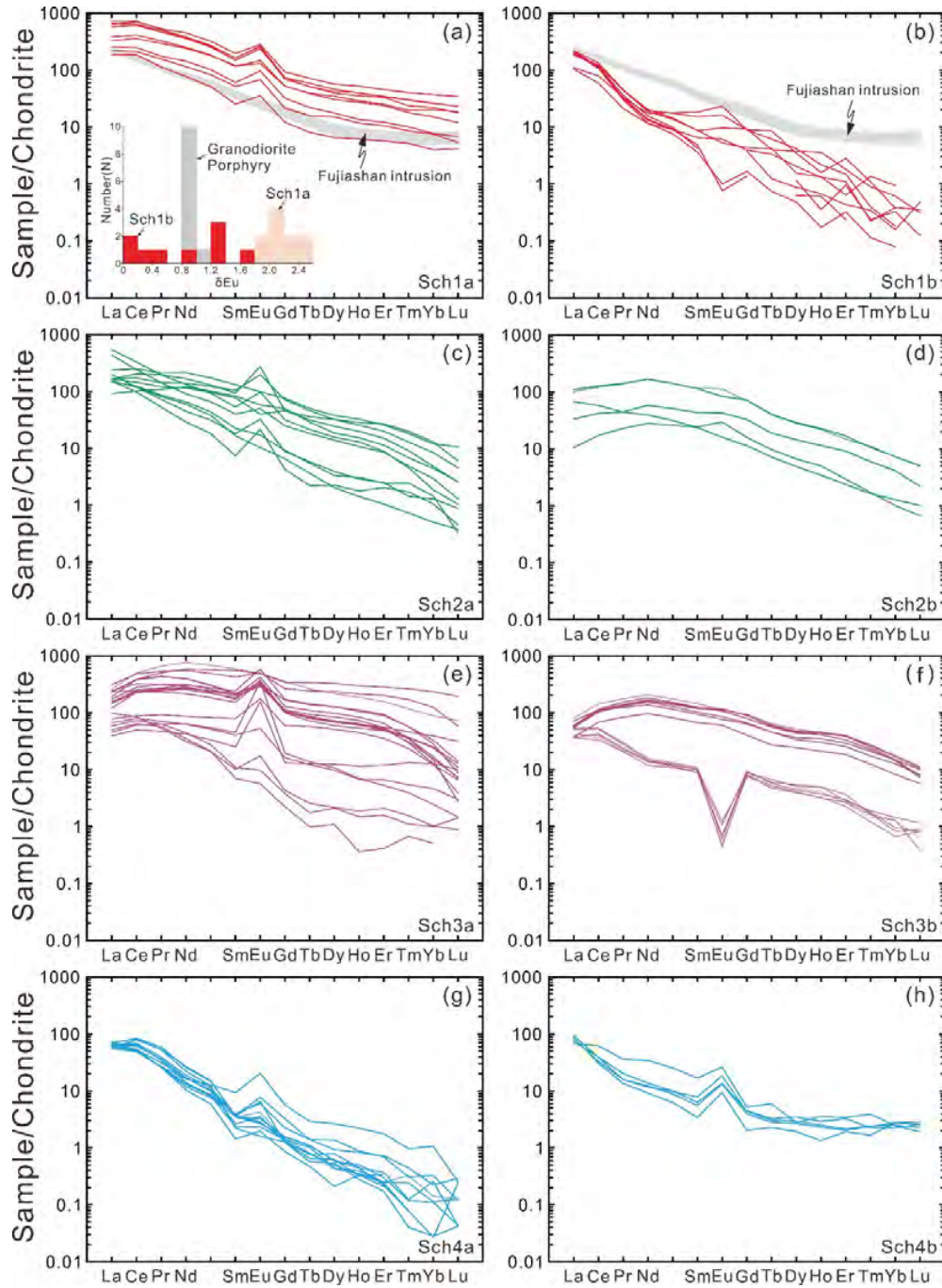
Figure 7
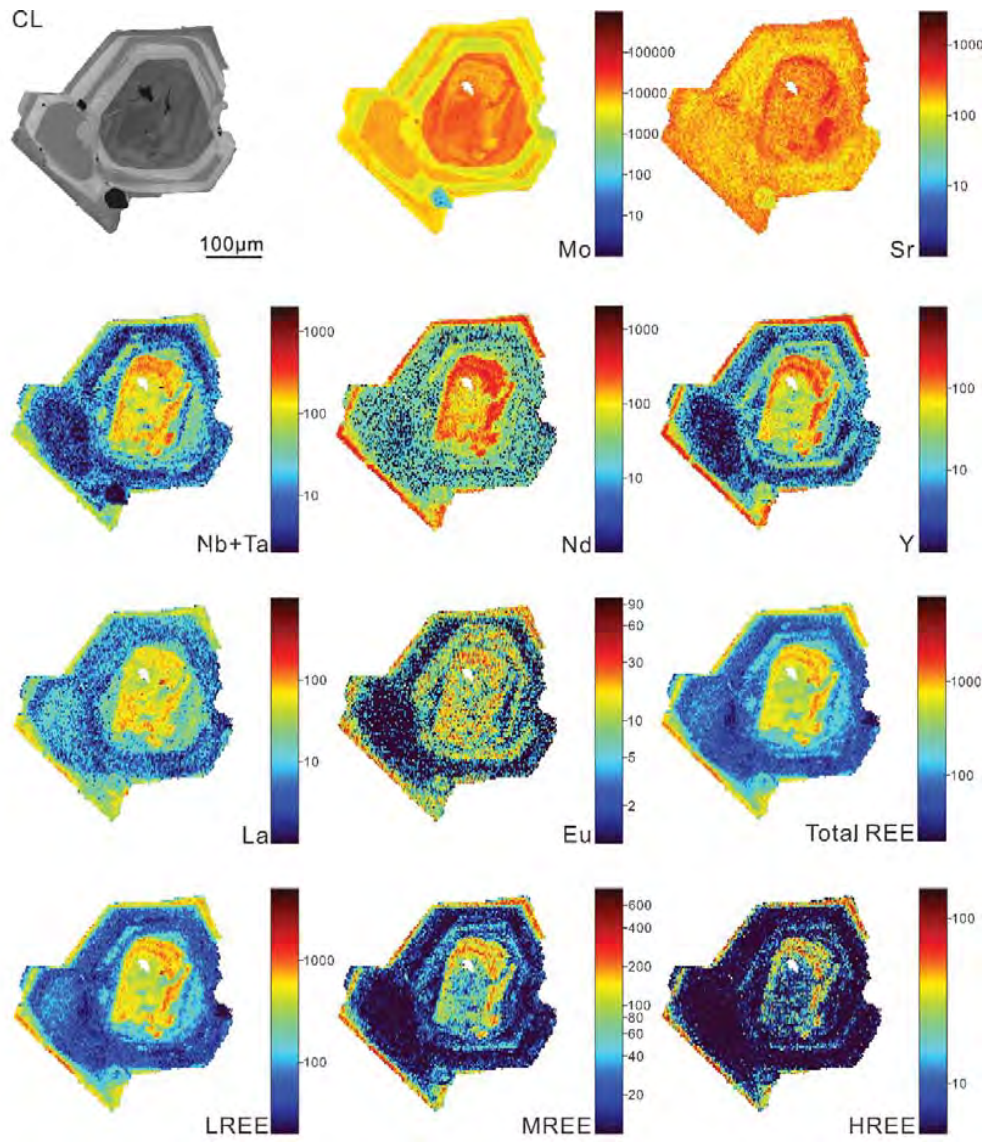
Figure 8
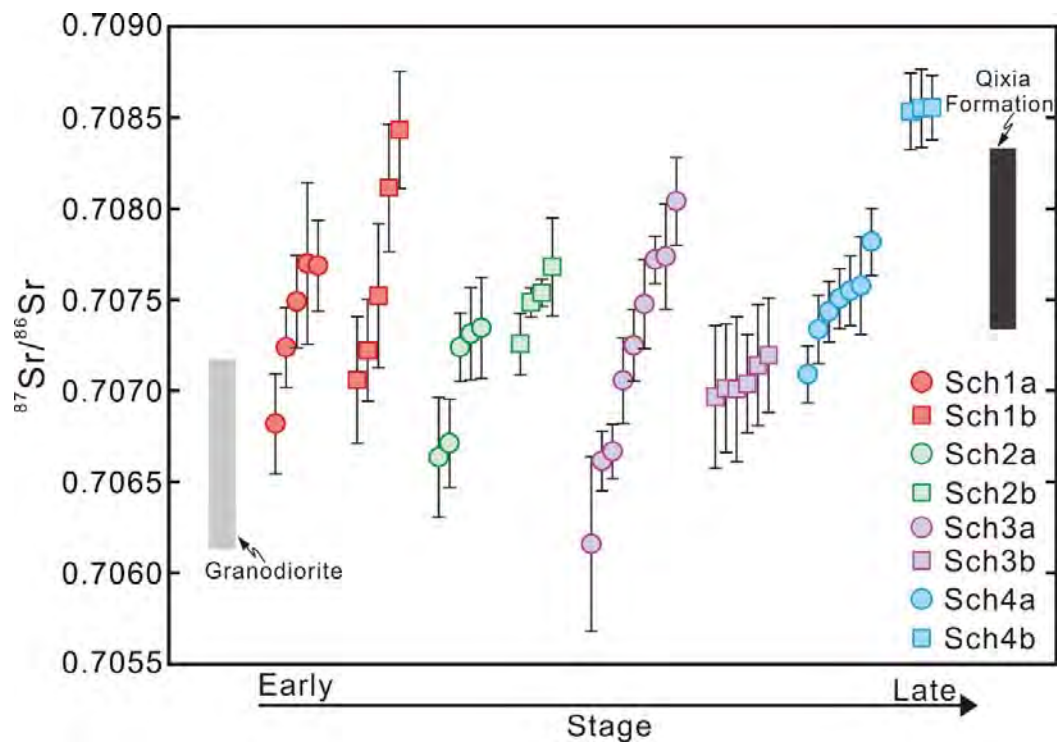
Figure 9

Figure 10

Figure 11

Figure 12

Figure 13